

PREPLANETARY NEBULAE: AN HST IMAGING SURVEY AND A NEW MORPHOLOGICAL CLASSIFICATION SYSTEM

RAGHVENDRA SAHAI¹, MARK MORRIS², CARMEN SÁNCHEZ CONTRERAS³, MARK CLAUSSEN⁴
 raghvendra.sahai@jpl.nasa.gov
Draft version February 3, 2008

ABSTRACT

Using the Hubble Space Telescope (HST), we have carried out a survey of candidate preplanetary nebulae (PPNs). We report here our discoveries of objects having well-resolved geometrical structures, and use the large sample of PPNs now imaged with HST (including previously studied objects in this class) to devise a comprehensive morphological classification system for this category of objects. The wide variety of aspherical morphologies which we have found for PPNs are qualitatively similar to those found for young planetary nebulae in previous surveys. We also find prominent halos surrounding the central aspherical shapes in many of our objects – these are direct signatures of the undisturbed circumstellar envelopes of the progenitor AGB stars. Although the majority of these have surface-brightness distributions consistent with a constant mass-loss rate with a constant expansion velocity, there are also examples of objects with varying mass-loss rates. As in our surveys of young planetary nebulae (PNs), we find no round PPNs. The similarities in morphologies between our survey objects and young PNs supports the view that the former are the progenitors of aspherical planetary nebulae, and that the onset of aspherical structure begins during the PPN phase (or earlier). Thus, the primary shaping of a PN clearly does not occur during the PN phase via the fast radiative wind of the hot central star, but significantly earlier in its evolution.

Subject headings: planetary nebulae, stars: AGB and post-AGB, stars: mass-loss, circumstellar matter

1. INTRODUCTION

Pre-planetary nebulae (PPNs), short-lived transition objects between the AGB and planetary nebula (PN) phases, probably hold the key to understanding how the slowly expanding ($5\text{--}15\text{ km s}^{-1}$), largely spherical, circumstellar envelopes (CSEs) of AGB stars (Neri et al. 1998) transform into highly aspherical PNs with fast outflows ($\gtrsim 100\text{ km s}^{-1}$) directed along one or more axes.

We are carrying out a program of multiwavelength imaging and spectroscopic observations of generally young PPNs, using a large (~ 300), morphologically unbiased sample (Sahai & Sánchez Contreras 2002, 2004), mostly constructed from catalogs of OH/IR stars (evolved, visually faint, mass-losing stars with dense circumstellar envelopes, showing, generally double-peaked, OH maser emission). Interferometric maps of the OH emission in many of the objects of this class (e.g. Bowers et al. 1983) show that it typically arises in an extended circular shell of radius $\sim 10^{16}\text{ cm}$, indicating that substantial AGB mass-loss has occurred through a spherical outflow. The IRAS spectral energy distributions (SEDs) of a large fraction of these objects indicate a lack of hot dust (25 to $12\mu\text{m}$ flux ratio $F_{25}/F_{12} > 1$, implying a lack of dust hotter than about 450 K), and therefore cessation of the dense AGB mass-loss process less than a few hundred years ago.

Here we report on our discoveries of objects with well-resolved geometrical structures from our imaging surveys of pre-planetary nebulae carried out using the Hubble Space Telescope (HST) in its SNAPshot mode. A previous SNAPshot survey providing images of resolved neb-

ulocities in 21 PPNs was carried out by Ueta, Meixner & Bobrowsky (2000). We use the large sample (>50) of PPNs now available (which includes previously-imaged objects in this class) to devise a new morphological classification system for this category of objects. We also derive post-AGB and AGB mass-loss time-scales, as well as dust masses, for our objects. The main focus of this paper is the morphology of PPNs; a more comprehensive statistical analysis which includes results on the unresolved and undetected objects in our surveys is deferred to a future paper.

2. OBSERVATIONS

The images presented in this paper were obtained as part of two SNAPshot survey programs with HST. The target lists for these programs were generated by selecting sources from published catalogs of OH/IR stars (te Lintel Hekkert et al 1988, 1991, 1992, Chengalur et al. 1993, te Lintel Hekkert & Chapman 1996, Hu et al. 1994, Likkel 1989, Sevenster et al. 2001, 1997a,b) which had strong emission ($\geq 0.8\text{ Jy}$) in the OH maser-lines (1665, 1667, and/or 1612 MHz) and with $F_{25}/F_{12} > 1.4$. A small number of additional objects were selected from the compilation of evolved stars with Low-Resolution IRAS spectra by Kwok, Volk & Bidelman (1997), subject to the same IRAS color criterion as for the OH/IR stars. This subset included carbon-rich (C-rich) objects and class H objects (showing a red continuum with either a $9.7\mu\text{m}$ silicate absorption feature or a $11.3\mu\text{m}$ PAH emission feature in their LRS spectra).

¹ Jet Propulsion Laboratory, MS 183-900, California Institute of Technology, Pasadena, CA 91109

² Department of Physics and Astronomy, UCLA, Los Angeles, CA 90095-1547

³ Dpto. de Astrofísica Molecular e Infraroja, Instituto de Estructura de la Materia-CSIC, Serrano 121, 28006 Madrid, Spain

⁴ National Radio Astronomy Observatory, 1003 Lopezville Road, Socorro, NM 87801

A $25\mu\text{m}$ flux threshold of 25 Jy was then imposed in order to exclude relatively distant objects. This yielded a sample of about 200 objects. The Digitized Sky Survey (DSS) optical images, available from the online databases maintained by the Canadian Astronomy Data Centre, were used to examine a $3 \times 3 \text{ arcmin}^2$ field-of-view around each object in order to check whether any bright field stars were present very close to our target which would make their imaging difficult. Objects for which no visual detection could be made on the DSS plates were excluded. The USNO-B.1 and the Guide Star Catalog II (GSC-II) were queried to determine R magnitudes; when these were unavailable, a rough assessment of the R magnitude was made from the DSS images. The remaining sample was divided into 3 magnitude bins (bright: $R < 13$, medium: $14 < R < 17$, and faint: $R > 17$), and roughly equal numbers of objects were randomly selected from each bin in order to meet the target limitation of 117 objects for the two survey programs, GO 9101 (17 objects) and 9463 (100 objects), described below. A small number of targets which represent the evolutionary phases just preceding and following the PPN phase were also included in these two programs.

Both programs were carried out in the SNAPshot mode of HST in which objects are selected from the program source list to fill gaps in the general observational schedule, thus all objects in the list were not observed. The first survey program, GO 9101, was a pilot survey with WFPC2 in which 10/17 objects were imaged. The second, GO 9463, was a more extensive survey in which a total of 58/100 objects were imaged with ACS. For GO 9101, we obtained images using the F606W ($\lambda = 0.60\mu\text{m}$, $\Delta\lambda = 0.123\mu\text{m}$) & F814W ($\lambda = 0.80\mu\text{m}$, $\Delta\lambda = 0.149\mu\text{m}$) filters, with the 800×800 -pixel Planetary Camera (PC) of Wide-Field & Planetary Camera 2 (WFPC2), which has a plate scale of $0''.0456/\text{pixel}$. For GO 9463, we used either the High Resolution Camera (HRC) or the Wide-Field Camera (WFC) of the Advanced Camera for Surveys (ACS), depending on the optical magnitude of the object. The HRC has a plate scale of $0''.025/\text{pixel}$, and for objects imaged with this camera, we used a combination of the F606W filter ($\lambda = 0.60\mu\text{m}$, $\Delta\lambda = 0.123\mu\text{m}$) and the F814W filter ($\lambda = 0.80\mu\text{m}$, $\Delta\lambda = 0.149\mu\text{m}$) for the fainter objects, and the F435W ($\lambda = 0.43\mu\text{m}$, $\Delta\lambda = 0.103\mu\text{m}$) and F606W filter for the brighter ones. The WFC has a plate scale of $0''.050/\text{pixel}$, and for objects imaged with this camera, we used a combination of the F606W filter and F814W filters. We also examined the HST archive for additional PPNs which met our IRAS color and flux selection criteria (and not published previously). We found one such object, IRAS 15553-4230 (GO 10627, PI: M. Meixner) which was imaged with the ACS/HRC – we have included it in this paper.

Some of the objects from GO 9463 were also imaged as part of our GO 9801 program – a third survey to image optically-faint PPN candidates with Camera 1 or 2 of the Near Infrared Camera and Multi-Object Spectrometer (NICMOS) using two or three of the F110W ($\lambda = 1.1\mu\text{m}$, $\Delta\lambda = 0.55\mu\text{m}$), F160W ($\lambda = 1.6\mu\text{m}$, $\Delta\lambda = 0.4\mu\text{m}$) and F205W ($\lambda = 2.0\mu\text{m}$, $\Delta\lambda = 0.6\mu\text{m}$) filters. The complete results of this survey, which did not yield resolved images of any new PPN, will be discussed separately; in this paper

we utilise the NICMOS images when available for providing additional details on the morphology.

3. RESULTS

We have listed the sources in our survey in Table 1, with their 2MASS coordinates. The images of all resolved objects are shown in Figs.1-28. Optical spectroscopy, allowing spectral types of the central stars to be determined (either from the direct starlight if the central star is visible, and/or from the starlight scattered by nebular dust), is not available for all of our objects. However, we have carried out spectroscopic surveys of partially-overlapping samples of candidate PPNs selected in the same manner as for our imaging surveys, using the Palomar 60-inch (Sahai & Sánchez Contreras 2002, 2004) and Keck 10-m telescopes (Sánchez Contreras et al. 2003, Sánchez Contreras et al. 2007, in preparation), and we find that the observed objects do not show the rich emission-line spectra characteristic of planetary nebulae. For those objects where spectral types have been determined, either by us or others, the spectral types obtained typically span the B, A, F, and G spectral types, which are the typical spectral types for post-AGB central stars.

The majority of our objects are oxygen-rich (O-rich) due to their selection from OH-maser catalogs. Information about the source chemistry is provided in the descriptions of individual PPNs in § 4.

3.1. Morphological Classification System

The PPNs in our survey show a variety of morphologies. We therefore describe a systematic method of classifying these. In this morphological classification system, we have taken care to avoid using criteria that are based on a 3-dimensional interpretation of the nebular structures whose 2-dimensional projection is observed in our images. The main structural components of PPNs in order of importance are the lobes, the waist, and the halo. Hence, we classify our objects into various morphological classes with the prime discriminant being the lobe structure. The presence or absence of a waist and halo are included as secondary descriptors. The classification system is described below, and the classification codes are summarised in Table 2. In Table 3, we apply these codes to the objects from our survey, and in Table 4, to previously imaged PPNs.

First, we divide the observed primary morphologies into 4 major classes – bipolar (B), multipolar (M), elongated (E), and irregular (I). There is no class referring to round shapes, because we have not found any object in which the central post-AGB structure appears round. The “bipolar” or B shape is defined by objects which show two primary, diametrically opposed lobes, centered on the central star (or center of mass if a binary system) or its expected location (e.g., IRAS 13557-6442, Fig.4; IRAS 15452-5459, Fig.6). The pair of lobes must have a “pinched in” shape in the region around the center from where they emanate, and/or the lobes should be visible on both sides of a minimum-light-intensity central region (presumably due to an obscuring dust lane, see below). The “multipolar” or M shape is defined by objects having more than one primary lobe on either side of the center (IRAS 19024+0044, Fig.15; IRAS 19475+3119, Fig.19). The “elongated” or E shape is simply one which is elongated along a specific axis, i.e.,

is not round (e.g., IRAS 17253-2831, Fig.9; IRAS 18420-0512, Fig.14). The “irregular” or I shape is defined by objects in which extended circumstellar structure can be seen, but where no obvious lobe or shell-like structures can be identified, and which therefore do not fit in any of the previous categories (e.g., IRAS 11385-5517, Fig.1). As the name implies, objects in the I category usually do not display axial or point-reflection symmetry.

Secondary structural features are denoted with lower-case letters following the major class. First, we add sub-classifications which are related to the lobes in the B, M, or E classes – these may be open (i.e., like a vase) or closed (i.e., having a bubble-structure) at their outer ends, and are denoted by *o* or *c*. For sources where the morphology is not sufficiently well-resolved or the images are too noisy to make the *o* or *c* determination, this subclassification is not mentioned. For multipolar (i.e., M) objects, where it is possible in principle to have some lobes which are open and some which are closed, both *o* and *c* should be used.

Some PPNs show bright, compact knots in diametrically-opposed pairs, normally referred to as ansae (e.g. as in IRAS 09371+1212, the Frosty Leo Nebula: Morris & Reipurth 1990, Sahai et al. 2000a) – these are denoted by *an*. Sometimes minor lobes can be seen, at low or intermediate latitudes, as, e.g. in the Egg Nebula (Sahai et al. 1998a), and the Frosty Leo Nebula – these are denoted by *ml*. The presence of a skirt-like structure around the primary lobes (as, e.g., in Hen 3-401, Sahai, Bujarrabal, & Zijlstra 1999a) is denoted by *sk*. This structure is an illuminated surface lying outside the primary bipolar lobes but with the same axis of symmetry; the skirt has a larger opening angle than the primary lobes, and while it surrounds these lobes it does not have as large a radial extent. Skirt structures are most easily discerned when the nebular axis is near the plane of the sky. But if the nebular axis is sufficiently inclined towards us, it may become difficult to distinguish between a waist with a sharp edge and a skirt. We discuss this issue in §5.5.

If there is a dark obscuring band that cuts across the center of the nebula (i.e. a minimum in an intensity cut taken along the primary long axis of the nebula, and usually described as the “waist” of the nebula), its presence is denoted by *w*. The dusty waist may be due to (i) an opaque dust torus that blocks light that arises or is scattered from a central region, or (ii) a disk that never allows light from the central star to emerge in directions near the equatorial plane. However, our morphological classification does not distinguish between these possibilities.

For several PPNs, the waist appears to have a sharp outer (radial) edge or boundary – we denote this by adding (*b*) after *w*. This outer boundary can show up in two different ways. The first, and more common, way is when the boundary is seen as a dark, convex (relative to the center of the nebula) edge cutting across one of the primary lobes⁵. A prime example of a well-studied PPN with such a “dark-edged” waist is the Egg Nebula (Sahai et al. 1998a); in our study we also find clear examples in, e.g., IRAS 19024+0044 (Fig.15), IRAS 19292+1806 (Fig.17), & IRAS 22036+5306 (Fig.21). The second way is when the

waist boundary smoothly transitions from a dark feature seen against the bright lobes to a brightness feature seen against the sky (or faint nebular) background in equatorial regions on either sides of the lobes. The best examples of this phenomenon are provided by IRAS 17106-3046 (Kwok et al. 2000) and IRAS 04296+3429 (Sahai 1999, but see Oppenheimer et al. 2005 for a different interpretation).

If the central star can be observed (in any of the optical filters commonly used with HST for imaging PPNs), we add the symbol ***.

Next, if there is evidence for point-symmetry in the nebular structure, we denote it by *ps*. This classification is not applied to axially symmetric objects, even though axial symmetry is a special case of point-symmetry. The point-symmetry can be of three general types: (i) the presence of 2 or more pairs of diametrically-opposed lobes, denoted as *m* (e.g. IRAS 19475+3119, Fig.19), (ii) the ansae are distributed point-symmetrically about the center (e.g. as in Frosty Leo), denoted as *an*, and (iii) the overall geometrical shape of the lobes is point-symmetric (e.g. Hen 3-1475), denoted as *s*. These three types of point-symmetry are listed in parentheses after the *ps* symbol, e.g., *ps(m)* means a nebula which is point-symmetric by virtue of having 2 or more pairs of diametrically-opposed lobes. An object may possess more than one type of point symmetry: e.g., IRAS 19024+0044’s point-symmetry would be represented as *ps(m,an)* since it shows both the presence of pairs of diametrically-opposed lobes, as well as ansae in one of the lobe pairs which are point-symmetric (Sahai et al. 2005).

The presence of a halo is denoted with *h*, and an (*e*) is added after it if it has a non-round, or elongated shape. If the halo shape cannot be determined reasonably (e.g., if the halo is rather tenuous and the source lies in a field with bright nearby stars, as in the case of IRAS 17543-3102), we add (*i*) meaning that the shape is indeterminate. Thus the default halo shape is assumed to be round. The presence of arc-like structures in the halo, as for example seen in the Egg Nebula (Sahai et al. 1998b), is denoted by (*a*). Note that a halo may have a smaller visible radial extent than the nebular lobes in the images shown. However, this does not necessarily imply that the physical radius to which the halo can be detected is smaller than the lobes, it is a result of the more rapid radial decrease of the halo surface brightness compared to the lobes. With azimuthal averaging, the halo can be traced to radii beyond the radial extents of the lobes.

In a few bipolar PPNs, searchlight-beams which appear to emanate from the center, can be seen illuminating parts of the halo at high latitudes around the polar axis. Although the best example of this phenomenon is provided by the Egg Nebula (Sahai et al. 1998b), similar features have been seen in four other PPNs – IRAS 20028+3910 (Hrivnak et al. 2001), IRAS 17150-3224 (Su et al. 2003), IRAS 17245-3951 (Hrivnak et al. 1999) and IRAS 18276-1431⁶.

Note that in our system, the M or multipolar classification does not necessarily imply the point-symmetric subclass, denoted by *m*, even though for the two M objects

⁵ A detailed discussion of this issue is given in §5.5

⁶ IRAS 18276 is included in our survey; a detailed study of this object utilising the HST images shown here and other data has been presented by Sánchez Contreras et al. 2007

in our survey, IRAS 19024+0044 and IRAS 19475+3119, the lobes appear in diametrically-opposed (i.e. point-symmetric) pairs. The reason for this is that it may be possible for objects to have multiple lobes, all of which cannot be unambiguously grouped into diametrically-opposed pairs. Specific examples of such objects are the Starfish Twins (He 2-47 and M1-37), two young planetary nebulae with multiple lobes described by Sahai (2000).

Similarly, the B or bipolar classification does not necessarily imply w (i.e., the presence of a dusty waist), even though most B objects have dusty waists. Specific examples of objects which are bipolar, but don't show dusty waists in their images, are, IRAS 17440-3310 (Fig.11) and IRAS 19306+1407 (Fig.18). It is possible that these objects do have a dusty waist, but the waist is sufficiently tilted away from an edge-on orientation, and hence does not appear as an intensity-minimum between the two lobes.

We have applied the above system to some of the most well-resolved and best-studied PPNs to ensure that it captures the important morphological characteristics of these objects. Thus, the Egg Nebula has the classification Bcw(b),ml,h(e,a,sb); Frosty Leo is Bcw(b)*, an,ml,ps(m,an,s); Minkowski's Footprint, M 1-92 (e.g. Bujarrabal et al. 1998) is Bcw(b)*,an; and Hen 3-401 is Bow*,sk (Sahai, Bujarrabal & Zijlstra 1999a). The water-fountain PPN, IRAS16342-3814 (Sahai et al. 1999b) is classified as Bcw,ps(s).

3.2. Distances, Sizes, Ages, and Dust Masses

We have estimated the distances to our survey sources (D_L) assuming a fixed luminosity of $6000L_\odot$ for each object, rather than using kinematic distances determined from radial velocities because these objects can quite often have large and peculiar motions relative to the general galactic rotation. Both the above choices have been motivated by a VLBA proper motion study of the young PPN, IRAS 19134+2131. For this object, Imai, Sahai & Morris (2007) determine a trigonometric parallax distance of 8 ± 0.8 kpc, giving a luminosity of $5500L_\odot$, and a Galactic rotation velocity of $\sim 125 \text{ km s}^{-1}$, much slower than that given by the Galactic rotation curve at IRAS 19134+2131's location. Our choice of a fixed luminosity in our computations is not meant to imply that all PPNs have this same value of the luminosity, but simply to provide a convenient normalisation factor for the ages and masses. The values of these parameters can then be conveniently scaled in future studies when better distance determinations of individual objects become available.

The bolometric fluxes have been computed for each object by integrating the SED from the optical to far-infrared wavelengths, using published optical, JHK-band, MSX and IRAS fluxes. For all objects where the central star is not visible, the total flux for wavelengths $\lambda \lesssim 2\mu\text{m}$ is quite small. In objects where the central star is visible, this short-wavelength flux can make a significant contribution to the bolometric flux, hence our luminosity determination is somewhat affected by the unknown amount of

interstellar extinction.

For each PPN, we have estimated the radial extent of the central aspherical structure (in arcseconds), which presumably represents the post-AGB mass-loss (r_{PAGB}), and the radial extent of the halo (in arcseconds) surrounding this structure (when it is present), which presumably represents the AGB mass-loss (r_{AGB}). For closed lobes, r_{PAGB} is measured radially outwards from the geometrical center of the nebula (or the central star, when visible) out to the most distant lobe structure along the lobe axis. If the lobes are "open" at their ends, then r_{PAGB} is defined as the radial offset of the most distant point on the lobe. If several lobes are present, or if the lobes on either side of the center have different lengths, the longest one is selected. For objects classified as I, i.e. when lobe structures are not visible, r_{PAGB} is defined as the radius to the most distant non-spherical structure. We have used azimuthal averaging to measure radial extent of the halos⁷. The azimuthal averages are done carefully in order to avoid the angular regions which are occupied by the nebular lobes. If a halo cannot be detected, we make the reasonable assumption that $r_{AGB} = r_{PAGB}$, motivated by the fact that the lobes result from the interaction of a fast AGB wind with a surrounding AGB envelope.

A post-AGB time-scale, t_{PAGB} ⁸, is derived by converting r_{PAGB} from angular units to linear units using the luminosity-based distances, and dividing it by a nominal outflow speed of 150 km s^{-1} (which is typical of the outflow speeds derived for the lobes of individual well-studied PPNs), since individual outflow speeds for the material in the lobes of most objects have not been measured as yet, nor are the inclination angles of the lobe axes well known. In objects with a halo, an AGB mass-ejection time-scale (t_{AGB})⁹ is computed by dividing the linear radius of the halo ($r_{AGB} \times D_L$) by the expansion velocity as derived from molecular line data (either OH 18 cm maser line or CO millimeter-wave line emission). Since the outer radius of the halo is most likely determined by the steadily decreasing halo surface-brightness falling below the noise (due to a decrease in density as well as central illumination), r_{AGB} , and correspondingly, t_{AGB} , should be understood as lower limits. By using azimuthal averaging, we can trace the halos out to significantly larger radial distances than possible with pencil-cuts of the intensity. The values of r_{AGB} given in Table 3 thus found are typically much larger than can be seen in the displayed images, where the intensity scales and stretches are chosen in order to display the central aspherical structures most clearly.

We have fitted the SED of each object from the near-infrared (K-band) to the far-infrared (as defined by MSX and IRAS fluxes) using a multi-component model (Sahai et al. 1991). A power-law (λ^{-p} , with $p=1.5$) dust emissivity with a value of $150 \text{ cm}^2 \text{ g}^{-1}$ (per unit *dust* mass) at $60 \mu\text{m}$ (Jura 1986) is used to fit the SED with a "cool", a "warm", and a "hot" component. The mass of the cool component, which is robustly fitted since the bulk of the emission comes from cool dust, is significantly larger than the other two components. This mass and the temperature

⁷ specifically, on a log-log plot of the averaged-intensity versus radius, the former drops smoothly out to r_{AGB} where it reaches the background-subtracted sky level and starts showing large fluctuations (either due to noise and/or the presence of many faint stars)

⁸ rounded to the nearest 5 yr in Table 3

⁹ rounded to the nearest 50 yr in Table 3

of the cool component, are therefore reported in Table 1. Comparison of the results of our simple models with those utilising radiative transfer codes to determine the temperature distribution in detail (e.g., for IRAS 19475+3119) indicate that the simple model gives dust masses that are lower than the more accurate values, by a factor 0.6-0.8.

We have found no obvious correlations between the morphologies and the post-AGB ages, dust shell masses or temperatures.

4. INDIVIDUAL SOURCES

IRAS 11385-5517 This object (HD101584), is well-known for its highly collimated, high-velocity bipolar outflow seen in OH maser emission (te Lintel Hekkert, Chapman & Zijlstra 1992) and massive molecular outflows (as seen in CO rotational line emission: Trams et al. 1990). The optical morphology is irregular (Fig.1). The central star has been classified as F0Iape (Hoffleit et al. 1983) and A6Ia (Sivarani et al. 1999, these authors contest Bakker et al. 1996's hotter, i.e., B9II, classification), and believed to be in a close binary (Bakker et al. 1996). Although the central star is heavily saturated in both images and produces a significant PSF contribution (e.g. radial streaks), the nebular structure is easily discernible, since all features which do not change their radial distance from the center as a function of wavelength have an astrophysical origin (Fig.2). The red- and blue-shifted OH 1667 MHz emission features define an axis of bipolarity with PA= -60° (te Lintel Hekkert et al. 1992).

IRAS 13428-6232 This object appears to be rather extended, with a bright cylindrical-shaped lobe seen in the F814W image on the southwest side; the inner parts of a very faint counterpart can be seen on the northeast side (Fig.3). The geometry is intrinsically bipolar, as can be seen in JHK images from the 2MASS archive and a K-band image by van de Steene, van Hoof & Wood (2000). The near-IR images show both lobes of the bipolar nebula very clearly. The cylindrical lobes are significantly more extended as seen in the 2MASS images: e.g., the K-band image (Fig.3) shows that the brighter (southern) lobe extends to about $24''.7$ along the nebular axis, compared to about $15''.7$ in the HST F814W image. The dusty waist has a flared shape in the K-band image, compared to the F814W image, where its edge bordering the southwest lobe is quite straight. This change in shape is easily understood as resulting from a decrease in the disk optical depth with wavelength from 0.8 to $2\mu\text{m}$. The central star of the nebula is clearly visible in the K-band image in van de Steene et al (2000) which has smaller pixels ($0''.25$) than the 2MASS image ($1''.0$). The nebula is much fainter in the F606W image. Therefore, although it has been listed as a possible young PN by Preite-Martinez (1988), the lack of nebulosity in the F606W filter (which covers the H α line) shows that any H α emission, if present, is very weak, indicating that the circumstellar material has not been ionised substantially. In the compilation by Kwok et al. (1997), the LRS spectrum of IRAS 13428 is classified as "H", i.e. having a red continuum with either a $9.7\mu\text{m}$ silicate absorption feature or a $11.3\mu\text{m}$ PAH emission feature, so its chemistry is unknown.

IRAS 13557-6442 This object is bipolar, with an hourglass shape and a dense waist seen almost edge-on (Fig.4).

The hourglass nebula is surrounded by an extended round halo. Using azimuthal averaging, we can trace the halo out to a radius of $\sim 3''$; the radial distribution roughly follows a power-law, $r^{-\beta}$ with $\beta \sim 2.3$. In this source, the MSX6C fluxes are roughly a factor 1.7 – 1.5 higher in the 12-21 μm range compared to the corresponding IRAS fluxes (either due to variability or poor calibration). We have therefore scaled down the MSX6C fluxes by a factor 1.6 in generating its SED. Since the blue and red peaks of the OH maser emission line are separated by only 3 km s^{-1} , it is unlikely that the standard interpretation of this separation representing twice the recent AGB CSE expansion velocity is applicable. We have therefore assumed $V_{exp}=15\text{ km s}^{-1}$, which gives an age $t_{AGB}=3200(D_L/3.3\text{ kpc})\text{ yr}$ for the halo.

IRAS 15405-4945 This bipolar nebula shows complex, highly structured lobes (Fig.5). A faint elliptical halo can be seen in the F814W image. If the halo is due to a spherical AGB mass-loss envelope, the elliptical shape indicates that the AGB envelope is being indirectly illuminated by the lobes, and not by a central source, or that the light from the central source cannot get out to the larger distances at low latitudes. We also obtained NICMOS images with NIC1 in the F110W and F160W filters. Although the overall shape of the bipolar lobes in these near-IR filters is roughly similar to that in the optical ones, there are distinct differences. The central star is visible in the NIC1 images, lying midway on the line joining the tips of the lobes. The OH masers in this object span a very large range (80 km s^{-1} in the 1612 MHz line, 105 km s^{-1} in the 1665 MHz line and 155 km s^{-1} in the 1667 MHz line), and lie along a PA of -45° , covering an elongated region with major axis of $\sim 2''$ (Zijlstra et al 2001). Thus the extent of the fast outflow as traced by the OH masers matches the size of the bipolar nebula seen in the HST images. We estimate an expansion velocity of the AGB envelope of 13.5 km s^{-1} from the separation of the prominent peaks in the OH 1665 MHz line profile; and given the $3''$ extent of the halo, we find $t_{AGB}=5200(D_L/4.9\text{ kpc})\text{ yr}$.

IRAS 15452-5459 This object shows a very extended hourglass shaped nebula in the F814W image; almost no nebulosity is visible in the F606W image. The two lobes are of roughly equal brightness and are separated by a flared, edge-on waist (Fig.6). We also obtained NICMOS images with NIC2 in the F110W, F160W and F205W filters – the shape of the extended nebula appears quite similar in all three near-IR filters compared to that in the F814W filter. However, the central star, which is not visible in the F814W image, appears visible at the geometrical center of the dust lane in the near-IR images. The waist, which appears as a minimum in intensity between the bright inner regions of the bipolar lobes, appears as a bright feature against the sky background beyond the western lateral periphery of the lobes, and shows a distinct, curved, outer edge. The OH maser emission in this object shows blue and red peaks at -67.2 and -48.3 km s^{-1} , implying an outflow speed of 9.5 km s^{-1} . Since a halo is not observed directly, we have assumed $r_{AGB}=r_{PAGB}$ to compute an estimated AGB mass-loss time-scale, $t_{AGB}=9850(D_L/1.7\text{ kpc})\text{ yr}$.

IRAS 15553-5230 This object is bipolar, with an hourglass shape and a dense waist seen almost edge-on (Fig.7), very

similar to IRAS 13557. It was only imaged in F814W. No halo can be seen. No line emission (either CO or OH) has been detected from the object, and the AGB expansion velocity is unknown. Assuming a typical AGB outflow velocity of $V_{exp}=15 \text{ km s}^{-1}$, we find $t_{AGB}=1430(D_L/4.3 \text{ kpc}) \text{ yr}$. We do not know if IRAS 15553 is oxygen- or carbon-rich; although it is included in the compilation by Kwok et al. (1997), its LRS spectrum is classified as “H”, i.e. having a red continuum with either a $9.7\mu\text{m}$ silicate absorption feature or a $11.3\mu\text{m}$ PAH emission feature.

IRAS 16559-2957 This object (with an F5Iab:e central star: SIMBAD database) shows a compact nebula with filamentary structures on either side of a central, round core (Fig.8). The eastern filament emanates from the central core, whereas the western one is separated from the latter by a dark band, which most likely represents a tilted, dusty equatorial structure. Using azimuthal averaging, we can trace a tenuous halo out to a radius of about $3''.5$. The radial distribution follows a power-law, $r^{-\beta}$ with $\beta \sim 2.8$. Using an AGB envelope expansion velocity of 14.8 km s^{-1} derived from OH maser data, we find that the AGB envelope was characterised by a roughly constant mass-loss rate over a period $t_{AGB}=5850(D_L/5.2 \text{ kpc}) \text{ yr}$. *IRAS 17253-2831* This object has point-symmetrically shaped lobes, and is surrounded by an extended round halo (Fig.9). The OH maser 1612 MHz profile shows 2 prominent peaks at V_{lsr} velocities of -71.4 and -53.2 km s^{-1} (implying an AGB envelope expansion velocity of 9.1 km s^{-1}) the emission at velocities within these peaks is confined to a poorly resolved, roughly elliptical region of size about $0''.35$ (Zijlstra et al. 2001). Using azimuthal averaging, we can trace the halo out to a radius of $\sim 2''.7$; the radial distribution follows a power-law, $r^{-\beta}$ with $\beta \sim 2.9$, signifying a roughly constant mass-loss rate over a period $t_{AGB}=10800(D_L/7.7 \text{ kpc}) \text{ yr}$. Zijlstra et al. (2001) believe that there is a fast bipolar outflow based on the locations of maser features at velocities outside the main profile peaks, but do not provide a position angle which can be compared with that of the optical nebula in our HST images.

IRAS 17347-3139 The F814W image shows a bipolar nebula with collimated lobes separated by a dense waist; almost no nebulosity is visible in the F606W image. The lobes show significant differences from each other in their structure (Fig.10). We also obtained NICMOS images with NIC1 in the F110W (not shown) and F160W filters (Fig.10). The shape of the extended nebula appears quite similar in both near-IR filters compared to that in the F814W filter. The two lobes are rather asymmetric in shape and size, with the NW lobe being significantly longer in extent. The latter also shows a very bright, collimated feature in its innermost region (bottom left panel, Fig.10) located mid-way between the lateral boundaries of the lobe. This collimated feature opens into a Y-shape; the right hand fork of this Y-structure is significantly longer than the left-hand one, and extends along the body of the lobe along a curved trajectory which, when extrapolated, culminates at the bright, bow-shaped tip of this lobe. These collimated structures are indicative of the presence of a highly-collimated jet whose axis has precessed while it has sculpted out the NW lobe. A faint elliptical halo can be seen around the lobes in the F160W

image. Using azimuthal averaging, we can trace this halo out to a radius of $\sim 2''$. Although OH maser emission is detected, the line profile is weak and complex (Zijlstra et al. 1989), and does not allow us to determine an AGB expansion velocity. Therefore, assuming a typical AGB outflow velocity of $V_{exp}=15 \text{ km s}^{-1}$, we find $t_{AGB}=1950(D_L/3.1 \text{ kpc}) \text{ yr}$.

The detection of radio continuum from this object (Gregorio-Monsalvo et al. 2004) suggests that IRAS 17347-3139 may be approaching the young planetary nebula phase, or may already have become a very young planetary nebula (note that two other well known pre-planetary nebulae, M 1-92 and AFGL 618, also show radio continuum emission). Gregorio-Monsalvo et al. also find H_2O maser emission, with a double-peaked profile having a total width of about 9 km s^{-1} , which they associate with a central toroid.

IRAS 17440-3310 This object has point-symmetrically shaped lobes, and is surrounded by an extended round halo (Fig.11). In the F606W image, a few circular arcs can be seen in the halo at low contrast. Using azimuthal averaging, we can trace the halo out to a radius of $\sim 4''$; the radial distribution follows a power-law, $r^{-\beta}$ with $\beta \sim 3$. Using an AGB envelope expansion velocity of 14.6 km s^{-1} derived from OH maser data, we find that the AGB envelope was characterised by a roughly constant mass-loss rate over a period of $t_{AGB}=9850(D_L/7.6 \text{ kpc}) \text{ yr}$.

IRAS 17543-3102 This object shows a complex shape, with a central bright nebulous region, and two ansae located along a SE-NW axis. The bright region is located closer to the SE ansa. Each of the ansae are aligned tangentially to the long axis of the nebula, defined by the vector joining the mid-points of the ansae (Fig.12). A linear stretch of the F606W image, with the central region saturated to bring out faint structures, shows that the ansae define the ends of elongated, lobe-like structures. Two additional bright knotty structures can be seen, one located NE of the SE ansa, and another located NW of the central region but closer to the center than the NW ansa. Using azimuthal averaging, a faint halo can be traced out to a radius of $\sim 2''$. Because of the presence of a large number of stars in the vicinity of this object, including two rather bright ones within $1''.3$ and $1''.8$ of the center of the nebula, we cannot check whether or not the halo is round. The radial distribution follows a power-law, $r^{-\beta}$ with $\beta \sim 2$. The AGB expansion velocity is unknown, since the OH maser emission line from this object shows a single peak. Therefore, assuming a typical AGB outflow velocity of $V_{exp}=15 \text{ km s}^{-1}$, we find $t_{AGB}=4600(D_L/7.3 \text{ kpc}) \text{ yr}$. *IRAS 18276-1431* This object (with a K2/K3 spectral type central star: SIMBAD database) has a bipolar shape with a central dense, roughly edge-on waist (Fig.13) and an extended halo. The two lobes shows different shapes, and a pair of “searchlight beams” emanate from the fainter one. If the halo is due to a spherical AGB mass-loss envelope, the elliptical shape indicates that the AGB envelope is being indirectly illuminated by the lobes, and not by a central source, or that the light from the central source cannot get out to the larger distances at low latitudes. A detailed study of this object, including near-infrared imaging using Adaptive Optics from the ground, has been presented by Sánchez Contreras et al. (2007), and we have used

their results in Table 3, scaled appropriately for the small difference in distance values (3 kpc in this paper, 2.7 kpc in theirs). IRAS 18276 shows OH maser emission and is therefore O-rich.

IRAS 18420-0512 This object shows a central bipolar shape embedded inside an extended halo; the central star is visible (Fig.14). One, possibly two, secondary lobes with collimated shapes emanate from the central region. Faint, roughly circular, arcs can be seen in the halo. The red and blue maser peaks in the OH line profile are located at 116.0 and 93.1 km s⁻¹, giving an expansion velocity of 12.4 km s⁻¹. Using azimuthal averaging, the halo can be traced out to a radius of $\sim 3''$; the radial distribution follows a power-law, $r^{-\beta}$ with $\beta \sim 3$, signifying that the AGB envelope was characterised by a roughly constant mass-loss rate over a period of $t_{AGB} = 7600(D_L/6.6 \text{ kpc}) \text{ yr}$.

IRAS 19024+0044 Since a detailed multiwavelength study of this object, which has a multipolar morphology (Fig.15) and an early-G type central star, has been reported by Sahai et al. (2005), we briefly summarise the main characteristics here. The object shows at least six elongated lobes, two with limb-brightened point-symmetric ansae at their tips, and a faint round halo characterised with $\beta \sim 3.2$, surrounds the lobes. Since Sahai et al. (2005) assumed a radial-velocity distance of 3.5 kpc resulting in a luminosity of $2600 L_{\odot}$, we have scaled up the distance-dependent values given in Table 1 appropriately, from the values given by Sahai et al. (2005). IRAS 19024 shows OH maser emission and is therefore O-rich.

IRAS 19134+2131 The object belongs to the class of “Water-Fountain” nebulae – preplanetary nebulae with very high-speed jets seen in H₂O maser emission. I 19134 appears quite compact in the optical images, but is clearly elongated along PA = $\sim 94^\circ$ (Fig.16), which is consistent with the orientation of the bipolar H₂O jet (Imai et al. 2004, 2007). In spite of the limited resolution, there appear to be two lobes separated by an intensity minimum, hence we tentatively classify this as a bipolar object with closed lobes, and a waist. No significant halo was detected for this source.

IRAS 19292+1806 This object shows a bipolar shape (Fig.17). A faint elliptical halo can be seen in the F814W image. If the halo is due to a spherical AGB mass-loss envelope, the elliptical shape indicates that the AGB envelope is being indirectly illuminated by the lobes, or that light from the central source cannot get out to the larger distances at low latitudes. By azimuthal averaging, this halo can be traced out to a radius of $2''.5$. Using an AGB envelope expansion velocity of 10.5 km s⁻¹ derived from OH maser data, we find that $t_{AGB} = 4250(D_L/5.2 \text{ kpc}) \text{ yr}$.

IRAS 19306+1407 This object shows a bipolar shape, with roughly cylindrical lobes (Fig.18). The central star (spectral type B0:e, SIMBAD database) is directly visible, and the lobes are surrounded by a tenuous round halo. By azimuthally averaging, the halo can be traced out to a radius of $\sim 4''$; the radial distribution follows a power-law, $r^{-\beta}$ with $\beta \sim 3.3$. No OH maser data are available for this source. This source most likely has a mixed chemistry (i.e. shows both carbon- and oxygen-rich dust features): Hrivnak et al. (2000) find PAH features in its ISO spectra, and Hodge et al. (2003) who silicate features at 11, 19, and 23 μm . We have determined an

AGB expansion velocity of 14 km s⁻¹ from our OVRO CO J=1-0 survey (Sánchez Contreras & Sahai 2003) for this object, signifying that the AGB envelope was characterised by a roughly constant mass-loss rate over a period $t_{AGB} = 6650(D_L/4.9 \text{ kpc}) \text{ yr}$. Lowe & Gledhill (2006) find a dust mass of $8.9 \pm 5 \times 10^{-4} M_{\odot}$ using a distance of 2.7 kpc from detailed modelling. Their value, when scaled by the square of the ratio of our larger distance to theirs, i.e., $(4.9/2.7)^2$, gives a dust mass of $2.9 \pm 1.6 \times 10^{-3} M_{\odot}$, which is larger than, but consistent within uncertainties, with our value of $1.3 \times 10^{-3} M_{\odot}$ (Table 3).

IRAS 19475+3119 A detailed multiwavelength study of this object, including HST imaging, has been reported by Sahai et al. (2007); and an interferometric study of millimeter-wave CO line emission has been carried out by Sánchez Contreras et al. (2006). Hence we briefly summarise the main characteristics here. IRAS 19475 (F3Ib central star: SIMBAD database) has a quadrupolar shape (Fig.19) showing two bipolar elongated lobes emanating from the center of the nebula. One of the bipolar lobe pairs clearly shows detailed point-symmetric structure with respect to the central star. A faint, surface-brightness-limited, diffuse halo surrounds the lobes. Since Sahai et al. (2007) assumed a far kinematic distance of 4.9 kpc, at which this object has a luminosity of $8300 L_{\odot}$, we have scaled the values given by Sahai et al. (2007) for the distance-dependent parameters given in Table 1 appropriately. For the dust-mass, we use the study of Sarkar & Sahai (2006), and exclude the additional mass of large, cold grains derived from submillimeter-wave/millimeter-wave data for this object by Sahai et al. (2007). The ISO spectra of IRAS 19475 show that it is O-rich (Sarkar & Sahai 2006).

IRAS 20000+3239 This object is roughly elliptical in shape, and is surrounded by a prominent round halo (Fig.20). The radial brightness distribution in the halo can be roughly described by a segmented power-law, with an inner region extending to a radius of about $\sim 2''$ described with a power-law index $\beta \sim 2.3$, and an outer region which can be traced to a radius of about $5''$ and a power-law index $\beta \sim 4.2$. The age of the AGB envelope is $6850(D_L/3.5 \text{ kpc}) \text{ yr}$. The central star is classified as G8Ia, and the ISO/SWS spectra show it to be a C-rich object (Hrivnak et al. 2000).

IRAS 22036+5306 Since a detailed multiwavelength study of this O-rich PPN, which has an overall bipolar morphology (and an F5 [or earlier] central star), has been reported by Sahai et al. (2003), we briefly summarise the main characteristics here. The ACS images of this extended bipolar nebula (Fig.21) show the main structures imaged with WFPC2 previously (Sahai et al. 2003) – namely, the bipolar lobes with bright regions S1 and S2, the central ring-like dense waist (R_b and R_d), and the knotty linear structures labelled J_E and J_W in Sahai et al. (2003). In addition, the F814W image resolves the central star from surrounding bright nebulosity, and shows the presence of two ansae just beyond the tips of the main lobes as well as a faint round halo. The radial brightness distribution follows a segmented power-law, with an inner region described with a power-law index $\beta \sim 2.3$ and extending to a radius of about $\sim 3''$, and an outer region described by a power-law index $\beta \sim 4.4$, which can be traced to a ra-

dius of about $6''.5$. Sahai et al. (2003) argue for a distance of 2 kpc for this object, at which its luminosity is $2300L_{\odot}$, and the total (dust+gas) mass of the dominant shell component used to model the SED, about $4.7M_{\odot}$. Given this large mass, and a further large (but uncertain) mass contribution from an additional cold component estimated recently from IRAS 22036+5306's submillimeter and millimeter-wave continuum fluxes (Sahai et al. 2006a), it is unlikely that the object can be at the larger distance which corresponds to a luminosity of $6000L_{\odot}$. Hence for this object, we have retained a value of 2 kpc for its distance. We derive $t_{AGB}=8850(D_L/2 \text{ kpc}) \text{ yr}$ assuming an AGB expansion velocity of 7 km s^{-1} (derived from the central narrow component of the ^{13}CO line shown by Sahai et al. 2006).

IRAS 22223+4327 This object has a central round core, with two small lobes protruding on the southern side, and a single small lobe protruding on the northern side (Fig. 22). A prominent, smooth halo surrounds the central aspherical nebula. Faint, thin, partial shells can be seen within the halo in the F435W image, and to a lesser extent, in the F606W image. These structures cannot be fitted with concentric circles around the central star. Radial streaks due to the PSF of the central star are also present. The central star is classified as G0Ia in the SIMBAD database. Using azimuthally averaging, one can trace the halo out to a radius of $\sim 7''.5$; the radial distribution follows a power-law, $r^{-\beta}$ with $\beta \sim 3.8$, signifying that the AGB envelope is characterised by an increasing mass-loss rate over a period of $11000(D_L/4.3 \text{ kpc}) \text{ yr}$. The circumstellar envelope is classified as C-rich since it shows millimeter-wave HCN emission (Omont et al. 1993). The CO profile shows weak line wings extending over 50 km s^{-1} , indicating the presence of a fast post-AGB outflow.

IRAS 23304+6147 The object probably has a quadrupolar shape, although the two pairs of lobes are not as well separated, as, e.g., in IRAS 19475+3119. We tentatively classify it as M. The lobes are surrounded by a prominent round halo (Fig. 23). The radial distribution in the halo can be roughly described as a segmented power-law, with an inner region extending to a radius of about $\sim 2''.5$ described with a power-law index $\beta \sim 2.5$, and an outer region which can be traced to a radius of $\sim 5''.5$ and a power-law index $\beta \sim 3.8$. The age of the AGB envelope is $7000(D_L/4.2 \text{ kpc}) \text{ yr}$. The central star is visible, and is classified as G2Ia in the SIMBAD database. It has molecular carbon absorption features and is therefore C-rich (Hrivnak 1995). This object is thus remarkably similar to IRAS 20000+3239 in the properties of its post-AGB and AGB ejecta, except for its primary morphological classification, which is M, whereas IRAS 20000+3239 is E.

4.1. Related Objects: Nascent Preplanetary Nebulae & Young Planetary Nebulae

We included a few objects in our survey, which, from the evolutionary standpoint, bracket the pre-planetary evolutionary phase, the main focus of our surveys. Thus, we included two very late AGB stars, one which is O-rich (IRAS 01037+1219: also WX Psc, IRC+10011), and another, which is C-rich (IRAS 23166+1655: AFGL 3068). Our observations of IRAS 01037+1219 show a central, asymmetrical, elongated (oval-shaped) nebulosity in the

F814W image. The object appears much fainter and more compact in the F606W image (Fig. 24). The peak brightness region is also elongated and non-stellar (Fig. 25). We believe that this object has just begun the transition to the PPN phase and we label it as a “nascent PPN”, or nPPN. The distance and dust-shell related parameters (Table 3) for IRAS 01037 are taken directly from the detailed modelling study by Vinkovic et al. (2004), and have not been re-scaled to our standard luminosity value of $6000L_{\odot}$.

Other well-studied objects which belong to the nPPN class include the carbon stars IRC 10216 (Skinner, Meixner & Bobrowsky 1998), CIT-6 (Schmidt et al. 2002) and V Hydrae (Sahai et al. 2003), all of which show strongly aspherical structures at their centers; a brief summary of an HST survey directed at this class is given by Sahai et al. (2006b). A detailed discussion of this class of objects is deferred to a future paper.

IRAS 23166+1655 does not show any bright central nebulosity or a central star; however, there is a substantial diffuse round halo with a large number of roughly circular arcs centered on the 2MASS coordinates of this object. The arcs and their interpretation have been discussed by Maunon & Huggins (2006) and Morris et al. (2006). Since there is no central organized structure, this object is not relevant for our morphological classification system.

We also included four young planetary nebulae, IRAS 17047-5650 (better known as CPD-56°8032), IRAS 21282+5050, IRAS 22568+6141 (Garcia-Lario et al. 1991), and IRAS 19255+2123 (better known as K 3-35), in our survey. IRAS 17047-5650 is a well-known dusty planetary nebula with a late WC central star (Crowther, de Marco & Barlow 1998). Its F435W image (Fig. 26) shows a multipolar object, with one well-defined set of diametrically-opposed bipolar lobes oriented roughly along a NE-SW axis; in a second pair oriented N-S, the northern lobe is observable to its tip, but the southern counterpart appears to be surface-brightness limited along its length, and its tip is not seen. There are complex brightness variations which likely represent additional geometrical structures, e.g., one may infer the presence of a shell oriented roughly along a NW-SE axis. The central star is visible in the image.

The PN IRAS 21282+5050 (Crowther et al. 1998) shows a morphology (Fig. 27) qualitatively very similar to that of CPD-56°8032 – it has two pairs of diametrically-opposed lobes, and a central roughly rhomboidal-shaped shell. Our F606W image of IRAS 22568+6141 (Fig. 28) shows a bipolar nebula with highly structured lobes; no central star can be seen. A compact bright ansa can be seen just south of the southeastern lobe, and it appears to be connected to this lobe via a narrow, jet-like feature. A counterpart to this elongated feature is seen marginally just north of the northwestern lobe. The overall shape of the lobes is roughly point-symmetric.

IRAS 19255+2123 is a well-studied dusty planetary nebula noted for being the first PN in which H_2O maser emission was found (Miranda et al. 2001); such PNs are exceedingly rare presumably due to the very short lifetime of H_2O masers during the PN phase. Its F606W image shows a bipolar nebula (Fig. 29); the north lobe, which is the brighter of the two, shows significant brightness structure, including a bright region on its eastern periphery

(B_N), that has a bright point-symmetric counterpart in the southern lobe (B_S). A bright ansa is seen at the tip of the southern lobe (A_S), with a possible counterpart at the tip of the northern lobe (A_N). A dense dusty waist separates the two lobes, and a diffuse halo surrounds the lobes at low and intermediate latitudes.

4.2. *IRAS 05506+2414: An Unrelated Object?*

The morphology of this object is unlike that of any PPN or PN, although it met the selection criteria for our survey. The HST image (Fig. 30) shows a bright compact knot (Sa), and a fan-like spray of elongated nebulous features (e.g. knots $K1-4$; not all the knots seen in the image have been labelled) which are separated from the former, but appear to emanate from it. A second compact knot (Sb) is seen to the west of the main source. We find that the MSX and 2MASS sources identified with the IRAS source are located at the position of knot Sa , indicating that it is associated with the stellar source powering an outflow that produces the knots $K1-4$ ¹⁰. A 1612 MHz OH maser source was discovered towards IRAS 05506 with the Arecibo dish (Chengalur et al. 1993) – the profile is not the typical double-peaked profile seen towards most dying stars. The main lines at 1665,67 MHz were detected by Lewis (1997) with peak fluxes of 300 and 150 mJy using Arecibo; the emission covers about 15 km s^{-1} in the 1612 MHz line and $\sim 40\text{--}45 \text{ km s}^{-1}$ in the main lines.

If IRAS 05506 is not associated with an evolved star, but instead is a young stellar object (YSO), then the OH maser observations argue for it not being a low-mass YSO, since there are no known OH masers toward low-mass YSOs. So if it is a YSO, it must be related to a high-mass star-formation region (SFR), suggesting the presence of an ultra-compact HII region with detectable continuum emission. However, the NVSS VLA all sky survey at 20 cm shows no continuum source towards IRAS 05506 down to an rms noise of $\sim 400 \mu\text{Jy/beam}$. Could IRAS 05506 then really be a PPN, but with a morphology which has never been seen before in PPNs or PNs? While this an improbable hypothesis, it is not implausible, considering that not so long ago, Sahai & Nyman (2000) discovered a planetary nebula with a bipolar, knotty jet, bearing an uncanny resemblance to jets seen in low-mass YSOs. A detailed discussion of the nature of IRAS 05506 is outside the scope of this paper; but will be presented, together with new optical, millimeter-wave and radio data in a forthcoming paper (Sahai et al. 2007, in preparation).

5. DISCUSSION

The morphological scheme we have presented in this paper is based on the PPNs in our survey and on additional well-studied PPNs outside our sample. Our PPN survey sample is a well-defined sample, but it is not a complete sample. We have listed in Table 4 all PPNs with high-resolution images in the literature outside our sample and we find that all of these can be accommodated within our classification scheme. Thus, Tables 3 and 4 list all known galactic PPNs with existing high-resolution images – a total of 53 objects. Many of the objects in Table 4 are taken from the PPN survey by Ueta et al. (2000). These authors classify PPNs as either SOLE (objects with bright central

star embedded in a faint extended nebosity) or DUPLEX (objects with bipolar shapes with a completely or partially obscured central star), and suggest that the *axisymmetry* in PPNs is created by an equatorially enhanced superwind at the end of the AGB phase. In view of the many very strong departures from axisymmetry in a very significant fraction of the full sample of PPNs, we do not think that the Ueta et al. classification provides a sufficiently complete framework for classifying the morphologies of PPNs.

5.1. *Pre-Planetary and Young Planetary Nebulae: Morphological Similarities*

The wide variety of morphologies which we have found are qualitatively similar to those found for young planetary nebulae in a previous HST survey (e.g., Sahai & Trauger 1998, Sahai 2000, Sahai 2003) and other ground-based studies. In particular, we find multipolar objects like IRAS 19024+0044, which closely resemble the “Starfish Twins” – two young PNs with multiple lobes (Sahai 2000). The quadrupolar object, IRAS 19475+3119, probably belongs to the class of quadrupolar planetary nebulae first identified by Manchado, Stanghellini & Guerrero (1991). In the “bipolar” class, the cylindrical lobe shape together with the associated very dense waist found in IRAS 13428-6232, is very similar to that of the well-studied PN IC 4406 (e.g., Sahai et al. 1991). The (bipolar) hourglass-shaped PPN, IRAS 15452-5459, resembles hourglass-shaped PN like MyCn 18 (Sahai et al. 1999c) and Hb12 (Sahai & Trauger 1998).

There are a few PPNs which are best described as elongated (class E). If the elongated morphology of these objects is because they have prolate ellipsoidal shapes, then we expect that they will evolve into the category of PNs which have been classified as elliptical in morphological schemes for PNs (e.g., Corradi & Schwarz 1995). Alternatively, these may be intrinsically bipolar but with (i) the polar axis sufficiently tilted towards us so that it is difficult to see the pinching-in of the lobes at their bases, or (ii) insufficiently resolved so that the pinching-in of the lobes at the base is not visible. A good example of possibility (i) is provided by IRAS 18420-0512 (Fig. 14), where the north-west lobe shows some evidence for being pinched-in on its northeastern periphery. As in the case of our surveys of young PNs with HST (Sahai & Trauger 1998, Sahai 2003), we found no round PPNs.

The similarity in morphologies between all PPNs observed with high spatial resolution and young PNs strongly indicates that (i) the former are the progenitors of aspherical planetary nebulae, and (ii) the onset of aspherical structure begins during the PPN phase (or earlier). Thus, the primary shaping of a PN clearly does not occur during the PN phase via the fast radiative wind of the hot central star, but significantly earlier in its evolution.

The morphological system for PPNs which we have presented can be adapted for young PNs directly. The broad-band optical (and near-infrared) images of PPNs show light scattered off dust grains in the circumstellar material. The interaction of the fast collimated wind from the central star of the PPN with the slowly-expanding, spherical, AGB mass-loss envelope, produces lobes with dense walls which consist mostly of swept-up AGB wind mate-

¹⁰ These knots are most likely Herbig-Haro objects

rial. The walls are overdense with respect to both the interiors and the exteriors of the lobes. The shapes of the nebular lobes, which are the brightest regions of PPNs, thus represent the shapes of the dense walls of the lobes, since the interiors of the lobes are tenuous as demonstrated by the frequent presence of limb-brightening in the lobes. This basic structure of the lobes in PPNs is reproduced in numerical simulations by Lee & Sahai (2003).

When the central star becomes hot enough to substantially ionise the circumstellar material, the nebular walls then appear as bright features in $H\alpha$ and forbidden-line emission (e.g. $[NII]\lambda\lambda 6548, 6583$). Note that because the optical-line emission is proportional to $n_e^2 l$, and thus, $n^2 l$ (where n_e and n are the electron and total density and l is the path length), whereas scattered-light intensity is proportional to $n l$, generally the brightness contrast between the nebular walls and its surroundings is likely to be higher for PNs than for PPNs. The lobe morphology, both in the PPN and PN phase, is a direct indicator of the geometrical shapes of the dense lobe walls, and therefore of the wind-wind interaction process which created them.

The only distinction which needs to be kept in mind when modifying the PPN classification scheme for PNs is related to the appearance of the waist region. Since most surveys of PNs have been carried out in emission-line filters, the waist quite often (but not always) appears as a bright feature, rather than a dark feature. Hence, unlike the case of PPNs, in our classification of young PNs, we will not define the waist in terms of a minimum in intensity along the long axis of the nebula. Indeed, the waist is often the brightest structural component of a bipolar or multipolar planetary nebula, which is understandable if we assume that the waist region has much more mass than the lobes. Note also that if the waist region is in expansion, then it will continue to flow radially outward from the star as a PPN evolves into a PN. The central regions of PNs with waists are thus, in general, expected to be more exposed and visible than those of the PPNs from which they evolve. Of course, very young PNs such as IRAS 22568+6141 (Fig. 28) and K 3-35 (Fig. 29) still have optically-thick waists fully or partially obscuring their central stars. A detailed morphological classification of the young PNs from the HST surveys described in Sahai & Trauger (1998) and Sahai (2003), which are presumably most closely related to PPNs in an evolutionary sense, will be presented in a future paper (Sahai & Morris 2007, in preparation).

5.2. Morphology and Nebular Chemistry

The “total” sample of PPNs with resolved morphologies listed in Tables 3 & 4 (our survey plus previously observed ones) includes objects with both oxygen-rich and carbon-rich chemistries, as well as a few which display mixed chemistry (i.e., show features representative of both carbon-rich and oxygen-rich chemistry). Although O-rich objects outnumber the C-rich ones, there is a substantial fraction of the latter (about 25%). Since the ratio of dusty O-rich stars to dusty C-rich stars, as estimated from a sample drawn from the IRAS PSC, is about 9 (Thronson et al. 1987), and these objects are presumably the

progenitors of dusty PPNs, C-rich PPNs are certainly not under-represented in our total sample of PPNs relative to their parent population. Within the total PPN sample, there does not appear to be any significant correlation of morphology with nebular chemistry.

5.3. Lobes

The variety of lobe shapes and structures seen in young PNs led to a new model by Sahai & Trauger (1998) for PN shaping, in which fast collimated outflows, operating during the PPN or very late AGB phase, are the primary agents in producing aspherical planetary nebulae. Hence, our morphological classification system puts considerable emphasis on including descriptors which are related to the shapes, structures and symmetries of the lobes.

An important example of this emphasis is the fairly detailed characterisation of point-symmetry in our classification scheme, based on the recognition that various subtypes of point-symmetry impose fairly strong constraints on specific formation mechanisms. This has been discussed in detail by Sahai et al. (2005) in a study of the PPN, IRAS 19024+0044. Briefly, the M and ps(m) classification of this object suggests a precessing *bipolar* jet, in which the fast outflow could be in the form of discrete blobs ejected in discontinuous episodes, or a high-velocity jet that discontinuously changes direction, leading to the sculpting of multiple lobes in different directions within the ambient AGB envelope. The presence of point-symmetric ansae at the tips of one of the lobe pairs, represented by the ps(an) descriptor, requires that the collimated outflow which produced these lobes must have changed its axis during its operation, although by much less than the angular separation between lobes. Thus the physical mechanism(s) which produces the collimated outflows must be able to accommodate two different time-scales, one associated with generating the point-symmetrical ansae within a lobe-pair, and one associated with generating the point-symmetrically distributed multiple lobes.

The *o* and *c* secondary classifiers (related to whether lobes are open or closed at their ends, respectively) provide another example of descriptors that raise some important questions related to the dynamical interactions believed to shape PPNs. Generally, post-AGB collimated winds or jets interacting with AGB circumstellar envelopes (e.g., Lee & Sahai 2003) will produce closed lobes as the fast wind sweeps up the ambient CSE material in front of it. If the density of the ambient material falls sufficiently rapidly with radius (e.g., as r^{-3} or more steeply, perhaps even in a discontinuous manner), and/or the fast wind turns off, reducing the ram pressure compressing the dense material at the tip of the lobe, the compressed layer will expand due to thermal pressure¹¹. Secondly, fragmentation of the compressed layer due to hydrodynamic instabilities may also occur. As a result of the above two effects, the end of the lobe could dissipate and become undetectable, leading to the open-lobe appearance. The bipolar PPN Hen 3-401, which shows lobes with tattered ends (Sahai et al. 1999c), is a possible example of fragmentation of the lobe-ends due to instabilities. But hourglass-shaped bipolar PPNs such as IRAS 13557 (Fig. 4) and IRAS 15452 (Fig. 6) which

¹¹ note, however, that since this material cools rapidly, the consequently relatively low sound speed compared to the much higher expansion speed, will limit the efficacy of this effect

have wide-open ends, show no obvious evidence of fragmented clumpy material. Furthermore, if c lobes evolve into o lobes over time then we would expect the former to have systematically smaller values of t_{PAGB} than the latter, but this does not seem to be the case from an inspection of our results in Table 3 (note, however, that our sample is still too small to make this a robust conclusion). Perhaps magnetic fields stabilize the lobe walls against fragmentation in some objects and not others, depending on the field strength and configuration. To summarise, a theoretical investigation of issues related to the formation of open and closed lobes using, e.g., numerical hydrodynamic simulations, is thus quite important for our general understanding of the formation of aspherical structure in PPNs.

5.4. Halos

The prominent halos surrounding the central aspherical shapes seen in many of our objects are direct signatures of the undisturbed circumstellar envelopes of the progenitor AGB stars. The halos generally have round or elongated shapes. It is quite plausible that objects with elongated haloes have AGB envelopes which are intrinsically round, but appear elongated because they are either being indirectly illuminated by the lobes, or the light from the central source cannot get out to the larger distances at low latitudes. The majority of these have surface-brightness distributions consistent with a constant mass-loss rate with a constant expansion velocity (e.g., IRAS 17253-2831, IRAS 17440-3310, IRAS 18420-0512, IRAS 19024+0044). But there are also examples of objects with varying mass-loss rates, with instances of both where the mass-loss rate was higher (IRAS 23304+6147), and lower (e.g., IRAS 19475+3119), in the past.

Three objects (IRAS 20000+3239, 22036+5306 & 23304+6147) show halos which require a 2-piece segmented power-law to describe the surface brightness. This implies somewhat discontinuous changes in the AGB mass-loss rate, if we assume that the envelope expansion velocity has remained constant¹². Comparing the three objects, we find the interesting result that in all of these, the power-law in the outer (inner) region is steeper (shallower) than that for a constant mass-loss rate. The implication is that for these objects, the mass-loss rate went through a maximum, first increasing over a period of ~ 3800 - 4800 yr, and then decreasing.

5.5. Waists

A significant fraction of preplanetary nebulae appear to have an optically thick concentration of dust in their equatorial plane, i.e., a waist. We refer to this dust distribution as a disk, setting aside the question of whether it is a bound, orbiting disk, or an equatorial concentration of dust in an outflowing wind. We have noted in our classification scheme that, in quite a few PPNs, the disk has a sharp radial edge, that is, a discontinuity in the extinction projected against the extended emission from the

reflection nebula¹³. The curvature of this discontinuity is typically convex relative to the nebula's center of symmetry, consistent with its being caused by radial structure in an axisymmetric disk.

This result carries interesting implications about the geometry of the disk. For the simple case of a bipolar nebula, for example, a sharp edge projected against the far lobe is a strong indication that the disk is density bounded at its outside edge. The sharp edge to the waist in that case is most likely due to the abrupt radial termination of the disk. If the surface density of dust in the disk were to fall off monotonically without an abrupt falloff (e.g., as $1/r$ for a disk that is radially outflowing at constant velocity and constant mass loss rate), then the edge would be relatively diffuse. These remarks apply to a situation in which the disk scale height increases with radius as would be expected for an outflowing disk. Examples of sharp edges are found in the well-studied PPNs such as AFGL 2688 (Sahai et al. 1998a), and in our sample objects IRAS 19292+1806 (Fig.17) and IRAS 22036+5306 (Fig.21).

Determination of which lobe of a bipolar nebula is the far lobe can be done by appeal to the kinematics; the rear lobe is the redshifted lobe. It is usually, though not always, the dimmer or more absorbed lobe because of extinction by the disk, but this is not a reliable indicator because the lobes may be intrinsically asymmetric (e.g., OH 231.8+4.2).

We note that it is possible to have a sharp edge against the near lobe of a bipolar PPN if several conditions are met: 1) the disk has a sharp surface boundary, 2) the scale height of the disk density distribution rises linearly or less rapidly than linearly with radius, and 3) the observer's line of sight is approximately tangent to that surface. The last condition implies that the observer be viewing the system from near the equatorial plane, which, in any case, is the best vantage point from which to be able to identify such a system as a bipolar or multipolar nebula.

It is also possible for the disk geometry to be arranged so that it gives a sharp edge against the far lobe even if the disk does not have a sharp outer boundary. The conditions for that, however, are quite restrictive: 1) a sharp disk surface boundary, 2) a disk scale height that reaches a maximum at some radius at which the disk is still optically thick, and 3) the observer's line of sight be tangent to the disk at the point where the disk reaches its maximum scale height. While this is possible, it is not well motivated physically, so we regard any object that shows a sharp radial edge projected against the far lobe as a case in which the disk has a sharp outer boundary.

The inferred sharp outer boundary to the disks in a number of systems can most easily be explained by an abrupt transition in mass loss geometry from spherically symmetric to an axisymmetric geometry having some combination of a latitude-dependent mass loss rate and a latitude-dependent outflow velocity. Models for such a transition can be based on the presence of a close binary companion (e.g., Morris 1987, 1990) or on the emergence of a strong stellar magnetic field after mass loss has stripped away

¹² It is unlikely that radial extinction of the illuminating light from the center plays a significant role in establishing a steep power-law index β for the surface brightness in the outer region, because if radial extinction was important, it would have an even more dramatic effect on steepening the power-law in the inner region

¹³ Because the waist regions are best seen when they are edge-on or close to edge-on, in which case one cannot determine from the images whether or not the disk is truncated at an outer radius, there is an observational bias against seeing waists with such outer edges

enough of the overlying stellar atmosphere (Blackman et al. 2001a,b). These issues will be discussed in a separate paper.

It is important to note that waists with sharp outer edges may not be distinguishable from skirt structures if the nebular axis is sufficiently inclined towards us. An example of this is provided by Hen 3-1475 (Fig. 31). A color image combining images taken through the F555W and F814W filters with WFPC2 clearly demarcates the waist/skirt structure – most prominently defined by a relatively red, sharp-edged elliptical band (feature labelled *W/Sk1* in inset, Fig. 31) which cuts sharply across the south-east or far lobe. South-east of *W/Sk1*, one can see a bluer structure whose outer edge is a partial ellipse (*W/Sk2* in inset) which joins *W/Sk1* near the equatorial plane. An apparent cusp can be seen on the south-west side of the nebula where *W/Sk1* and *W/Sk2* meet, suggesting a skirt structure for these features. However, since this cusp feature is not well-defined, and its counterpart on the north-east side is not apparent, we cannot definitively argue for the presence of a skirt in Hen 3-1475.

The central obscuring structure in OH231.8+4.2 (Fig. 32) is quite similar to that of Hen 3-1475, with its near-side seen as an obscuring elliptical band, partially cutting across the south-west nebular lobe and partially seen as a bright structure projected against the sky background (feature labelled *Sk1*). Its far-side counterpart is seen most clearly as a bright structure against the sky background on the eastern and western flanks of the bright south-eastern nebular lobe (*Sk2*). The skirt-shape can be inferred from the cusp resulting from the intersection of the projected edges of *Sk1* and *Sk2* on the north-western side of the nebula; a similar cusp can be seen somewhat less clearly on the south-eastern side. A quantitative analysis of the colors in the central region of these objects may help in better elucidating the structural relationship between the waist and skirt features.

6. CONCLUSIONS

Using the Hubble Space Telescope, we have carried out a survey of a well-defined set of candidate preplanetary nebulae. We present images of 22 new PPN and 1 nascent PPN with well-resolved geometrical structures. Combining this sample of PPNs with previously studied objects in this class, we have devised a comprehensive new morphological classification system for this class of objects. We summarize our major findings below:

(1) We have found a wide variety of aspherical morphologies which include bipolar and multipolar shapes, many of which display point-symmetries by virtue of their shapes and/or structures. This variety of morphologies is qualitatively similar to those found for young planetary nebulae in previous surveys. As in the case of our surveys of young planetary nebulae (PNs), we found no round PPNs.

(2) We also find prominent halos, surrounding the central aspherical shapes, in many of our objects – these are direct signatures of the undisturbed circumstellar envelopes of the progenitor AGB stars. The majority of these have surface-brightness distributions consistent with a constant mass-loss rate at a constant outflow velocity. But 3 objects require a segmented power-law to describe the surface brightness indicating that in these objects, the AGB mass-loss rate went through a maximum, first increasing over a period of ~ 3800 – 4800 yr, and then decreasing.

(3) We have estimated the physical sizes of the aspherical nebulae and the halos. Distances have been derived by measuring the bolometric flux of each object from its SED, and using a fixed luminosity of $6000L_{\odot}$. A time-scale for the duration of the post-AGB mass-loss (t_{PAGB}) and a lower limit to the time-scale for AGB mass-loss (t_{AGB}), have been derived from the expansion ages of the aspherical nebulae and the haloes, respectively, by making simplifying assumptions about the expansion speeds of the nebular material. A rather wide range of time-scales is found in both cases: t_{PAGB} lies in the range (30–1660) yr, with a median age of 180 yr, and t_{AGB} lies in the range (300–14700) yr, with a median age of 6650 yr.

(4) We have computed dust masses by fitting the SED of each object from the near-infrared (K-band) to the far-infrared (as defined by MSX and IRAS fluxes) using a simple multi-component model. The mass of the coolest component dominates the mass budget for each object. The dust masses cover the range $(0.53 - 23.5) \times 10^{-3} M_{\odot}$; the corresponding total masses, assuming a typical gas-to-dust ratio of 200, are $(0.1 - 4.7) M_{\odot}$.

(5) No obvious correlations are discernible between the morphologies and the post-AGB ages, dust masses, temperatures, or nebular chemistry.

(6) The similarities in morphologies between our survey objects and young PNs supports the view that the former are the progenitors of aspherical planetary nebulae, and the onset of aspherical structure begins during the PPN phase (or earlier). Thus, the primary shaping of a PN clearly does not occur during the PN phase via the fast radiative wind of the hot central star, but significantly earlier in its evolution.

RS and MM thank NASA for partially funding this work by a NASA LTSA award (no. 399-20-40-06); RS also received partial support for this work from HST/GO awards (nos. GO-09463.01-A and GO-09801.01-A) from the Space Telescope Science Institute (operated by the Association of Universities for Research in Astronomy, under NASA contract NAS5-26555). CSC is partially funded for this work by National Science Foundation grant 9981546 to Owens Valley Radio Observatory; the Spanish MCyT under project AYA2003-2785; and the Astrocam project (Ref: S-0505 ESP-0237).

REFERENCES

- Bakker, E. J., Lamers, H. J. G. L. M., Waters, L. B. F. M., & Waelkens, C. 1996, A&A, 310, 861
- Balick, B. & Frank, A. 2002, ARA&A, 40, 439
- Blackman, E.G., Frank, A., Welch, C. 2001a, ApJ, 546, 288
- Blackman, E.G., Frank, A., Markiel, J.A., Thomas, J.H., Van Horn, H.M. 2001b, Nature, 409, 485
- Bowers, P. F., Johnston, K. J., & Spencer, J. H. 1983, ApJ, 274, 733
- Bujarrabal, V., Alcolea, J., Sahai, R., Zamorano, J., & Zijlstra, A.A. 1998, A&A, 331, 361
- Chengalur, J. N., Lewis, B. M., Eder, J., & Terzian, Y. 1993, ApJS, 89, 189

- Cohen, M., Van Winckel, H., Bond, H. E., & Gull, T. R. 2004, *AJ*, 127, 2362
- Corradi, R. L. M., & Schwarz, H. E. 1995, *A&A*, 293, 871
- García Lario, P., Machado, A., Riera, A., Mampaso, A., & Pottasch, S. R. 1991, *A&A*, 249, 223
- de Gregorio-Monsalvo, I., Gómez, Y., Anglada, G., Cesaroni, R., Miranda, L. F., Gómez, J. F., & Torrelles, J. M. 2004, *ApJ*, 601, 921
- Hrivnak, B. J. 1995, *ApJ*, 438, 341
- Hoffleit, D., Saladya, M., Wlasuk, P. 1983, *Supplement to the Bright Star Catalog*, Yale University Observatory, USA
- Hrivnak, B. J., Volk, K., & Kwok, S. 2000, *ApJ*, 535, 275
- Hrivnak, B. J., Kwok, S., & Su, K. Y. L. 2001, *AJ*, 121, 2775
- Hu, J.Y., te Lintel Hekkert, P., Slijkhuis, S., Baas, F., Sahai, R., & Wood, P.R. 1994, *A&ASS*, 103, 301
- Imai, H., Morris, M., Sahai, R., Hachisuka, K., & Azzollini F., J. R. 2004, *A&A*, 420, 265
- Imai, H., Sahai, R., & Morris, M. 2007, *ApJ* (in press)
- Jura, M. 1986, *ApJ*, 303, 327
- Kwok S., Volk K., Bidelman W.P. 1997, *ApJ.Suppl.Ser.* 112, 557
- Kwok, S., Su, K. Y. L., & Hrivnak, B. J. 1998, *ApJ*, 501, L117
- Kwok, S., Hrivnak, B. J., & Su, K. Y. L. 2000, *ApJ*, 544, L149
- Lee, C-F. & Sahai, R. 2003, *ApJ*, 586, 319
- Lewis, B. M. 1997, *ApJS*, 109, 489
- Likkel, L. 1989, *ApJ*, 344, 350
- Lowe, K. T. E., & Gledhill, T. M. 2007, *MNRAS*, 374, 176
- Mauron, N., & Huggins, P. J. 2006, *A&A*, 452, 257
- Miranda, L. F., Gómez, Y., Anglada, G., & Torrelles, J. M. 2001, *Nature*, 414, 284
- Morris, M. 1987, *PASP*, 99, 1115
- Morris, M. 1990, in *From Miras to Planetary Nebulae: Which Path for Stellar Evolution?*, eds. M. O. Mennessier & A. Omont (Paris: Editions Frontieres), 520
- Morris, M. & Reipurth, B. 1990, *PASP*, 102, 446
- Morris, M., Sahai, R., Matthews, K., Cheng, J., Lu, J., Claussen, M., & Sánchez-Contreras, C. 2006, *Planetary Nebulae in our Galaxy and Beyond*, 234, 469
- Neri, R., Kahane, C., Lucas, R., Bujarrabal, V., & Loup, C. 1998, *A&ASS*, 130, 1
- Omont, A., Loup, C., Forveille, T., te Lintel Hekkert, P., Habing, H., & Sivagnanam, P. 1993, *A&A*, 267, 515
- Oppenheimer, B. D., Biegging, J. H., Schmidt, G. D., Gordon, K. D., Misselt, K. A., & Smith, P. S. 2005, *ApJ*, 624, 957
- Preite-Martinez, A. 1988, *A&AS*, 76, 317
- Sahai, R. 1999, *ApJ*, 524, L125
- Sahai, R. 2000, *ApJ*, 537, L43
- Sahai, R. 2003, *Planetary Nebulae: Their Evolution and Role in the Universe*, 209, 471
- Sahai, R., Wootten, A., Schwarz, H. E., & Clegg, R. E. S. 1991, *A&A*, 251, 560
- Sahai, R. & Trauger, J.T. 1998, *AJ*, 116, 1357
- Sahai, R., Hines, D.C., Kastner, J.H. et al., 1998a, *ApJ*, 492, L163
- Sahai, R., Trauger, J.T., Watson, A.M. et al., 1998b, *ApJ*, 493, 301
- Sahai, R., Bujarrabal, V., & Zijlstra, A., 1999a, *ApJ*, 518, L115
- Sahai, R., te Lintel Hekkert, P., Morris, M., Zijlstra, A., Likkel, L. 1999b, *ApJ*, 514, L115
- Sahai, R., Dayal, A., Watson, A.M., et al. 1999c, *AJ*, 118, 468
- Sahai, R., Zijlstra, A., Bujarrabal, V., te Lintel Hekkert, P. 1999d, *AJ*, 117, 1408
- Sahai, R. & Nyman, L-A 2000, *ApJ*, 538, L145
- Sahai, R., Bujarrabal, V., Castro-Carrizo, A., & Zijlstra, A. 2000a, *A&A*, 360, L9
- Sahai, R., Su, K.Y.L, Kwok, S., Dayal, A., & Hrivnak, B.J. 2000b, *ASP Conf. Ser.* 199, 167
- Sahai, R. & Sánchez Contreras, C. 2002, *BAAS*, 34, 1254
- Sahai, R., Morris, M., Knapp, G. R., Young, K., & Barnbaum, C. 2003, *Nature*, 426, 261
- Sahai, R., & Sánchez Contreras, C. 2004, *Asymmetrical Planetary Nebulae III: Winds, Structure and the Thunderbird*, 313, 32
- Sahai, R., Sánchez Contreras, C., & Morris, M. 2005, *ApJ*, 620, 948
- Sahai, R., Young, K., Patel, N. A., Sánchez Contreras, C., & Morris, M. 2006a, *ApJ*, 653, 1241
- Sahai, R., Morris, M., Contreras, C. S., & Claussen, M. 2006b, *Planetary Nebulae in our Galaxy and Beyond*, 234, 499
- Sahai, R., Sánchez Contreras, C., Morris, M., & Claussen, M. 2007, *ApJ*, 658, 410
- Sarkar, G., & Sahai, R. 2006, *ApJ*, 644, 1171
- Sánchez Contreras, C., Sahai, R., Gil de Paz, A., Goodrich, R.W. 2003, *BAAS*, 35, 1220
- Sánchez Contreras, C., & Sahai, R. 2004, *Asymmetrical Planetary Nebulae III: Winds, Structure and the Thunderbird*, 313, 377
- Sánchez Contreras, C., Bujarrabal, V., Castro-Carrizo, A., Alcolea, J., & Sargent, A. 2006, *ApJ*, 643, 945
- Sánchez Contreras, C., Le Mignant, D., Sahai, R., Gil de Paz, A., & Morris, M. 2007, *ApJ*, 656, 1150
- Schmidt, G. D., Hines, D. C., & Swift, S. 2002, *ApJ*, 576, 429
- Sevenster, M.N., Chapman, J.M., Habing, H.J., et al. 1997a, *A&AS*, 122, 79
- Sevenster, M.N., Chapman, J.M., Habing, H.J., et al. 1997b, *A&AS*, 124, 509
- Sevenster, M.N., van Langevelde, H.J., Moody, R.A. et al. 2001, *A&A*, 366, 481
- Sivarani, T., Parthasarathy, M., García-Lario, P., Machado, A., & Pottasch, S. R. 1999, *A&AS*, 137, 505
- Skinner, C.J., Meixner, M., & Bobrowsky, M. 1998, *MNRAS*, 300, L29
- Su, K. Y. L., Volk, K., Kwok, S., & Hrivnak, B. J. 1998, *ApJ*, 508, 744
- Su, K. Y. L., Hrivnak, B. J., & Kwok, S. 2001, *AJ*, 122, 1525
- te Lintel Hekkert, P., Caswell, J.L., Habing, H.J., Haynes, R.F., & Norris, R.P. 1991, *A&ASS*, 90, 327
- te Lintel Hekkert, P., Habing, H.J., Caswell, J.L., Norris, R.P. & Haynes, R.F. 1988, *A&A*, 202, L1
- te Lintel Hekkert, P., Chapman, J.M., & Zijlstra, A.A. 1992, *ApJ*, 390, L23
- te Lintel Hekkert, P., & Chapman, J.M. 1996, *A&ASS*, 119, 459
- Thronson, H. A., Jr., Latter, W. B., Black, J. H., Bally, J., & Hacking, P. 1987, *ApJ*, 322, 770
- Trams, N. R., Lamers, H. J. G. L. M., van der Veen, W. E. C. J., Waelkens, C., & Waters, L. B. F. M. 1990, *A&A*, 233, 153
- Ueta, T., Meixner, M., & Bobrowsky, M. 2000, *ApJ*, 528, 861
- Van de Steene, G. C., van Hoof, P. A. M., & Wood, P. R. 2000, *A&A*, 362, 984
- Vinkovic, D., Blocker, T., Hofmann, K-H., Elitzur, M., & Weigelt, G. 2004, *MNRAS*, 352, 852
- Zijlstra, A. A., Te Lintel Hekkert, P., Pottasch, S. R., Caswell, J. L., Ratag, M., & Habing, H. J. 1989, *A&A*, 217, 157
- Zijlstra, A. A., Chapman, J. M., te Lintel Hekkert, P., Likkel, L., Comeron, F., Norris, R. P., Molster, F. J., & Cohen, R. J. 2001, *MNRAS*, 322, 280

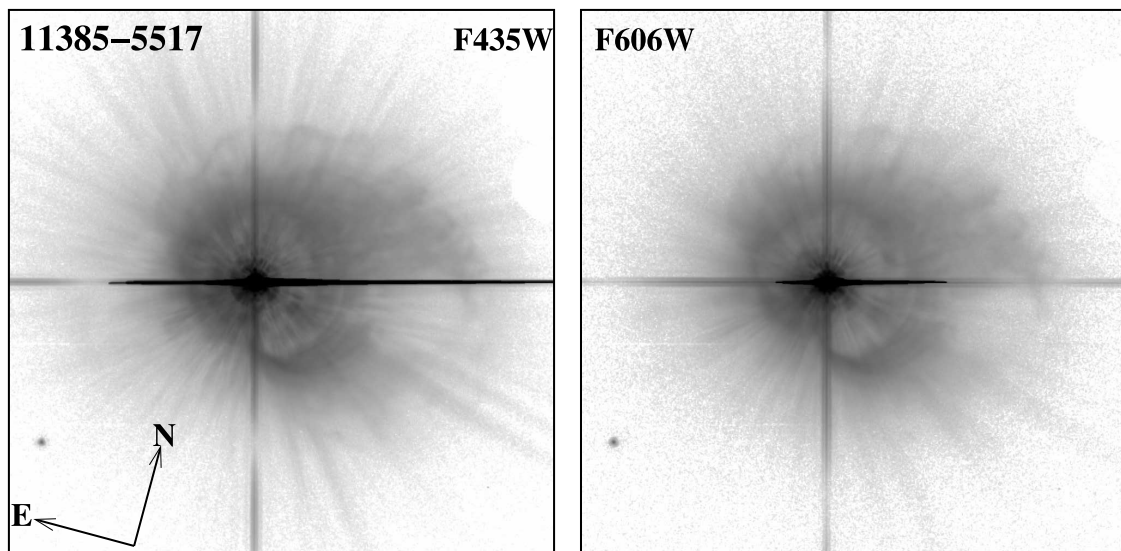


FIG. 1.— HST image (*log stretch*) of the young preplanetary nebula IRAS 11385-5517 ($12''.5 \times 12''.5$)

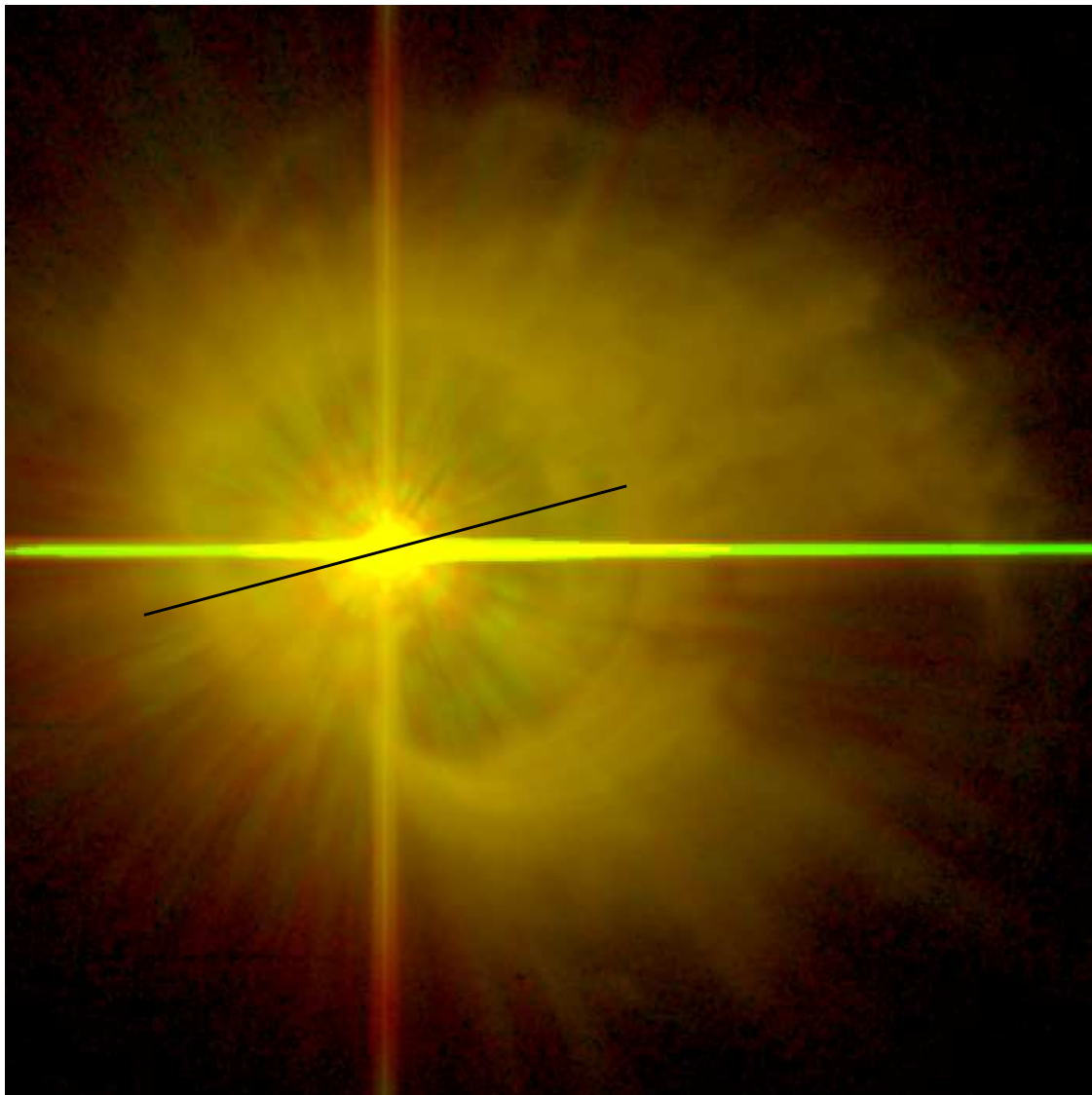


FIG. 2.— HST color-composite image (*log stretch*, *green*: *F435W*, *red*: *F606W*) of IRAS 11385-5517 ($8''.75 \times 8''.75$). Structures due to the PSF of the bright central star are readily apparent because corresponding PSF features in the two wavelength bands occur at slightly different radial distances, whereas real circumstellar structures overlap. The vector shows the orientation ($\text{PA} = -60^\circ$) and extent ($\pm 2''$) of the high-velocity bipolar OH maser outflow.

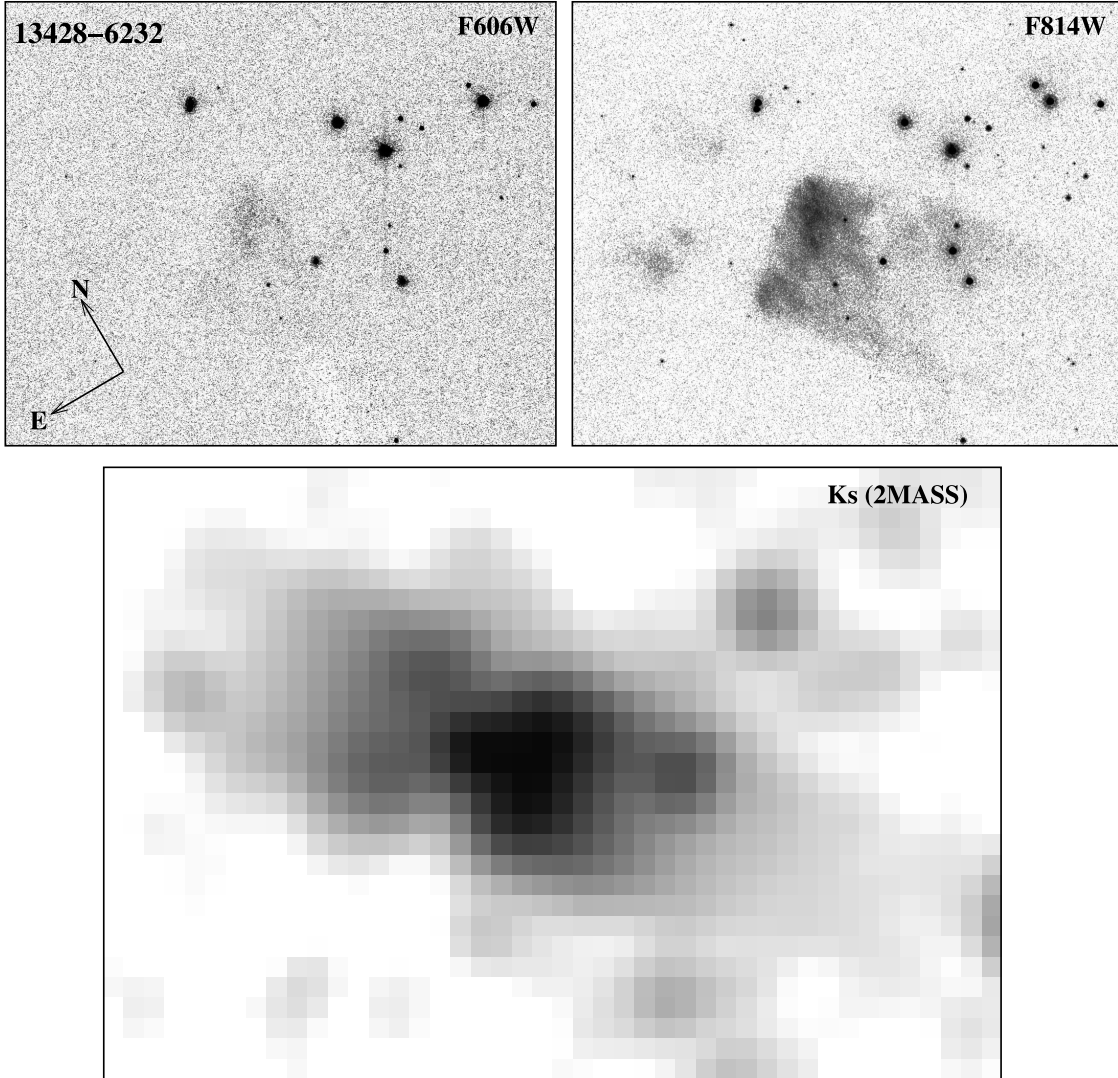


FIG. 3.— *top* HST images (*log stretch*) of the young preplanetary nebula IRAS 13428-6232 ($27''.0 \times 21''.75$); *bottom* K_s image from the 2MASS archive ($44''.0 \times 30''.0$)

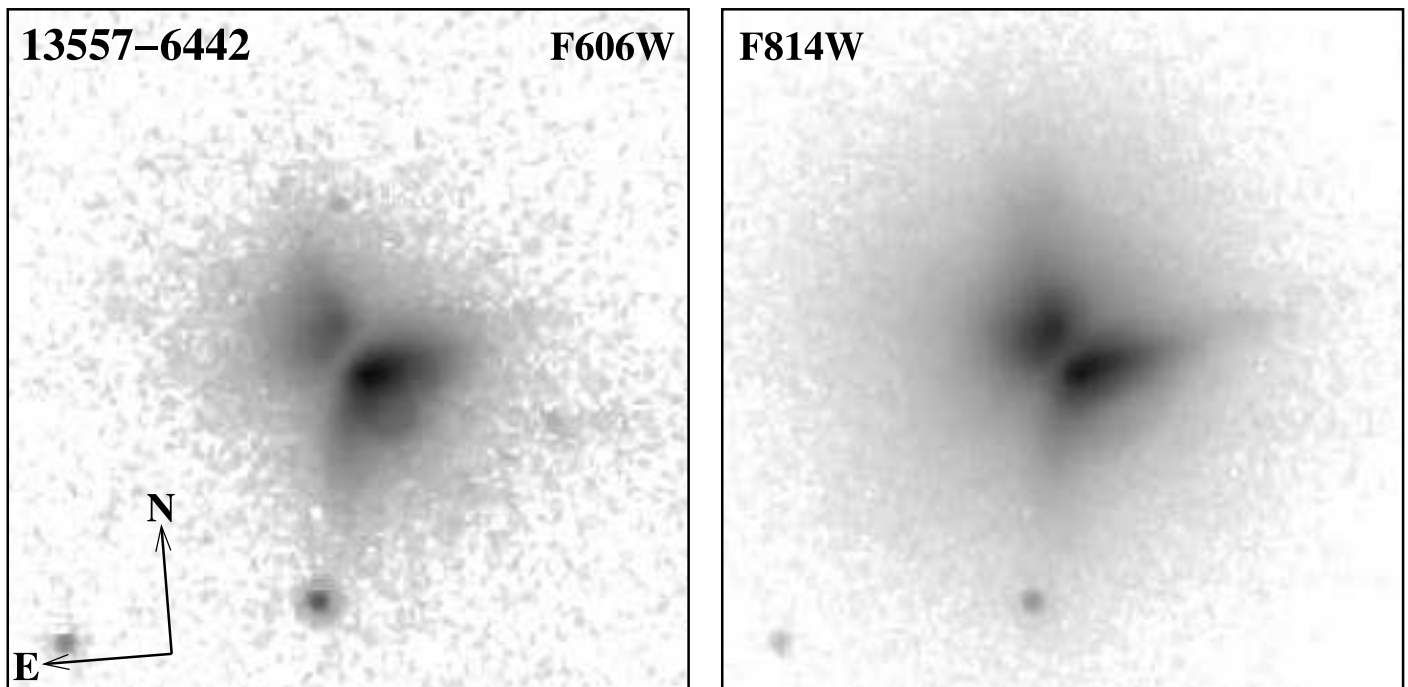


FIG. 4.— HST images (*log stretch*) of the young preplanetary nebulae IRAS 13557-6442 ($3''.125 \times 3''.125$).

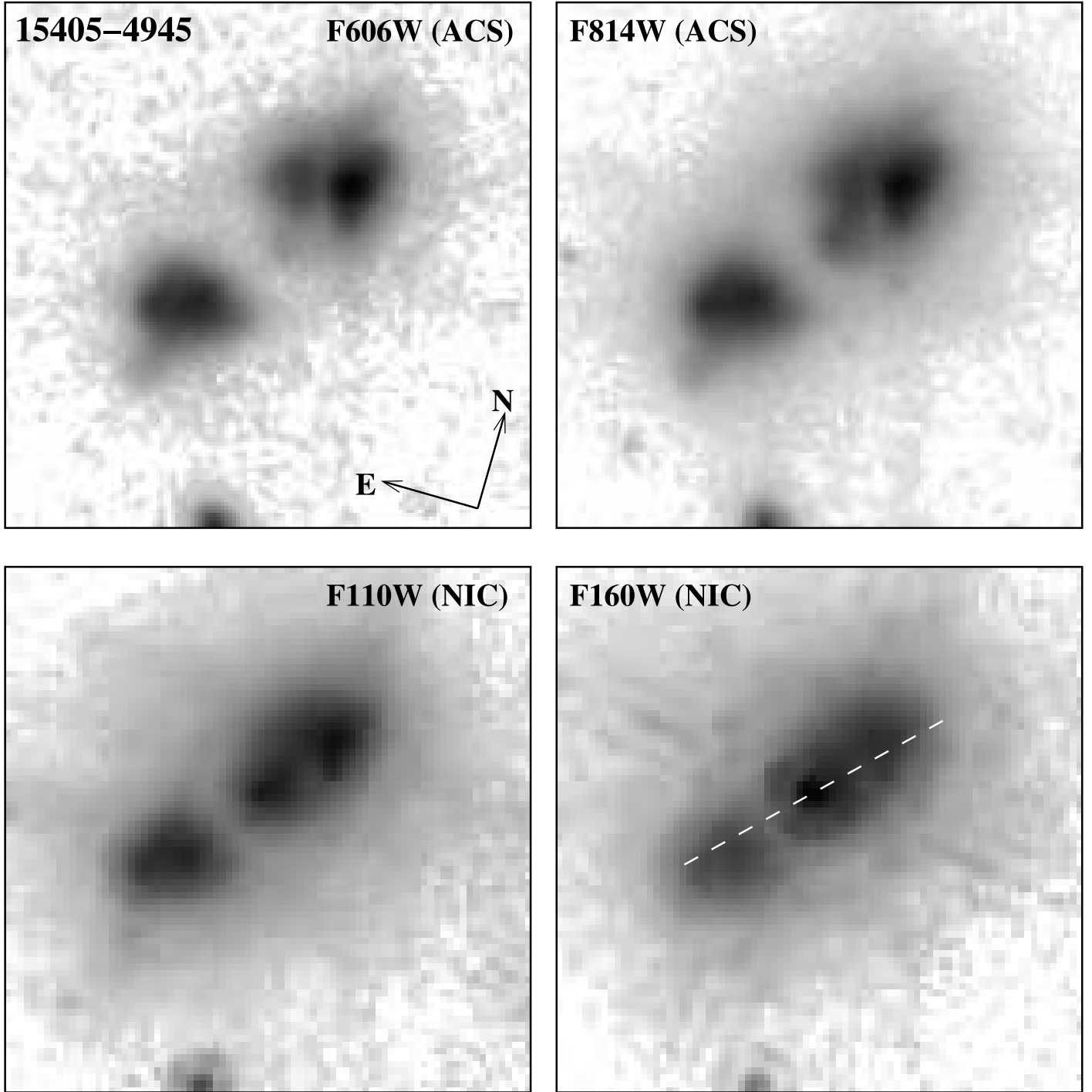


FIG. 5.— HST images (*log stretch*) of the young preplanetary nebula IRAS 15405-4945 ($3''5 \times 3''5$) — *top* ACS, *bottom* NICMOS. The dashed white vector shown in the F160W image denotes the PA (-45°) and extent of the bipolar outflow seen in OH maser emission by Zijlstra et al. (2001).

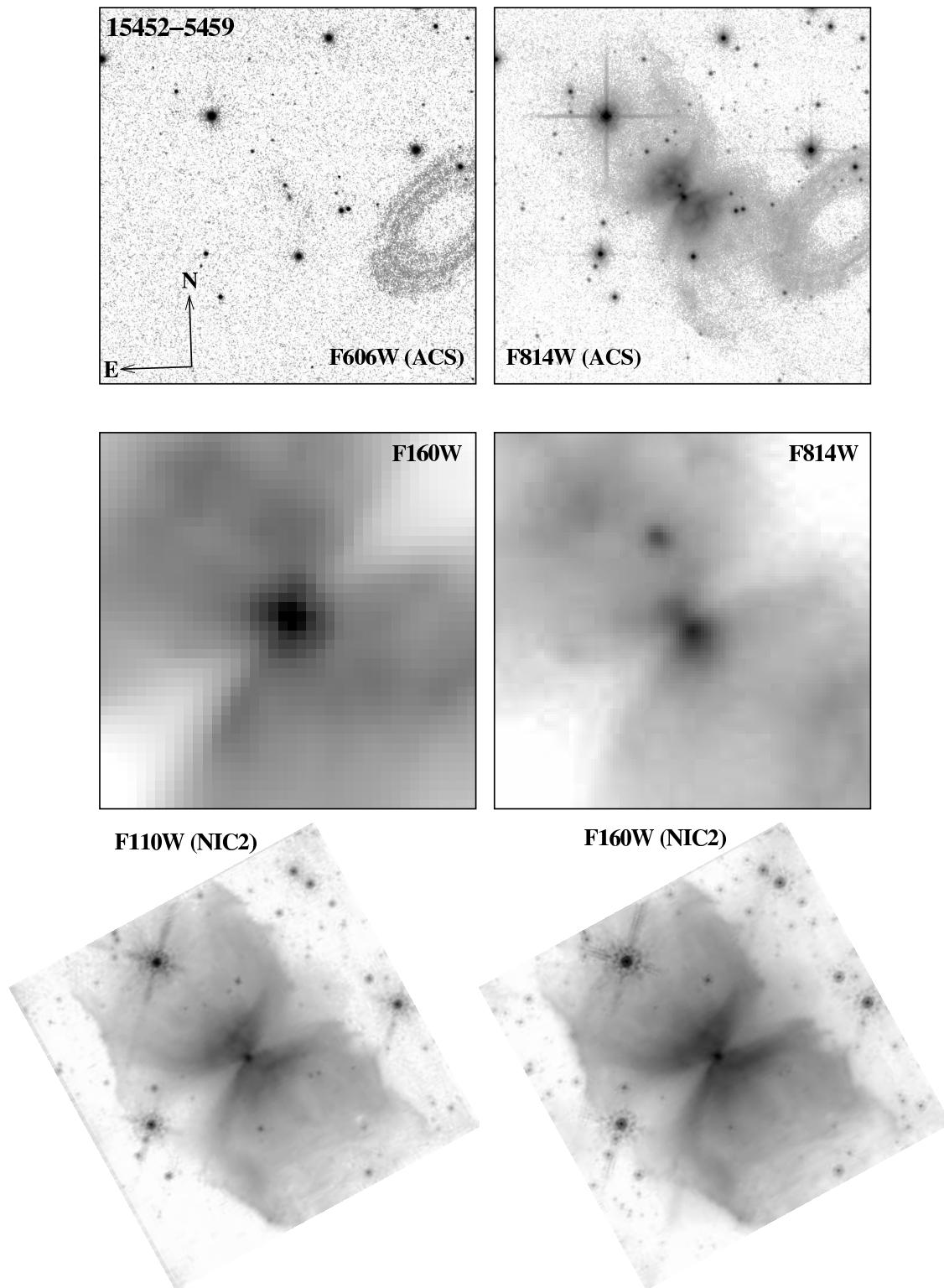


FIG. 6.— HST images (*log stretch*) of the young preplanetary nebula IRAS 15452-5459 *top* – extended nebula ($25''.0 \times 25''.0$ imaged with ACS (elliptical shape on the right hand edge of image is an instrumental artifact); *bottom* – extended nebula ($19''.3 \times 19''.3$) imaged with NICMOS, *middle* – central region ($3''.0 \times 3''.0$)

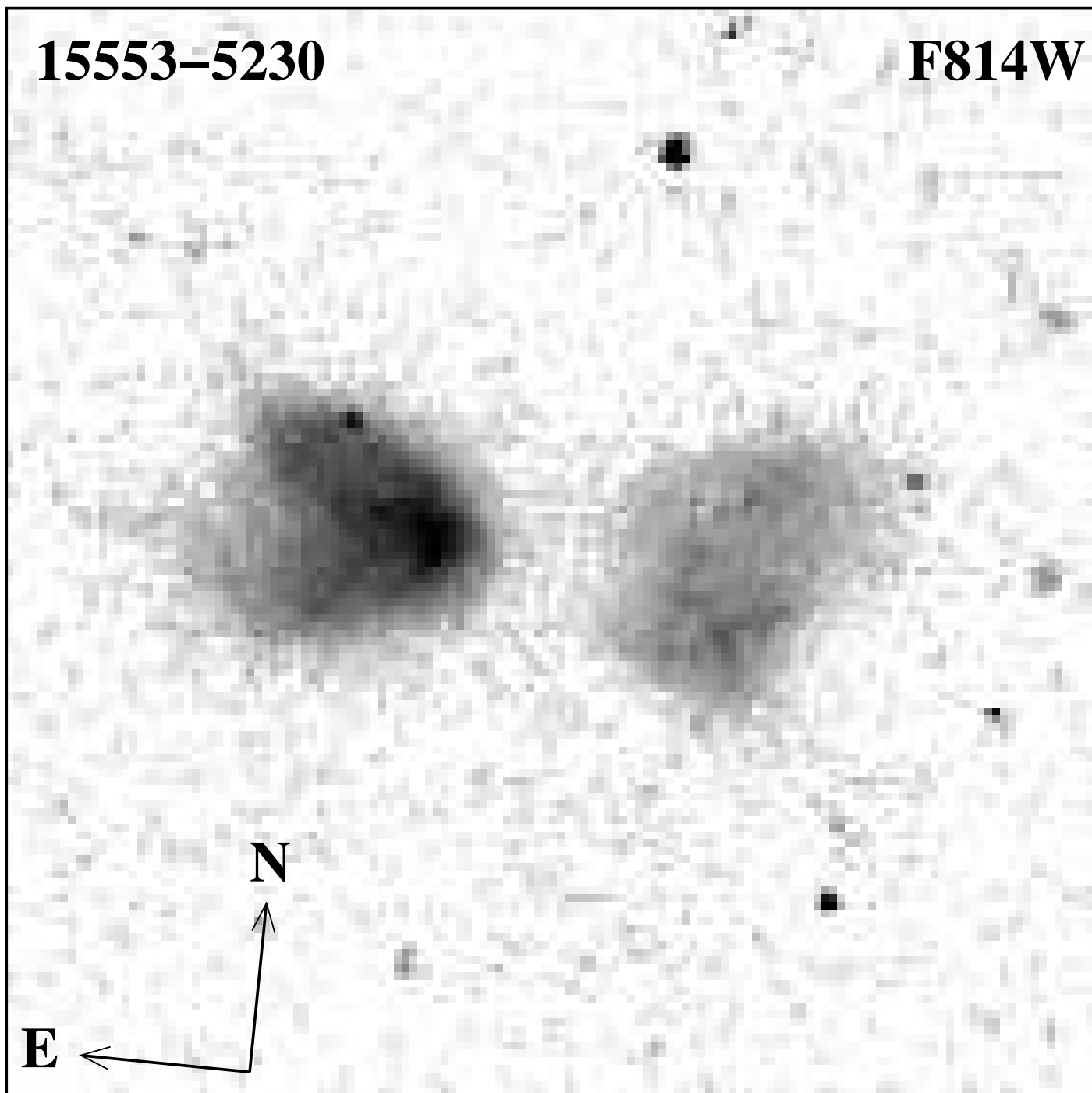


FIG. 7.— HST image (*log stretch*) of the young preplanetary nebula IRAS 15553-5230 ($3''.5 \times 3''.5$)

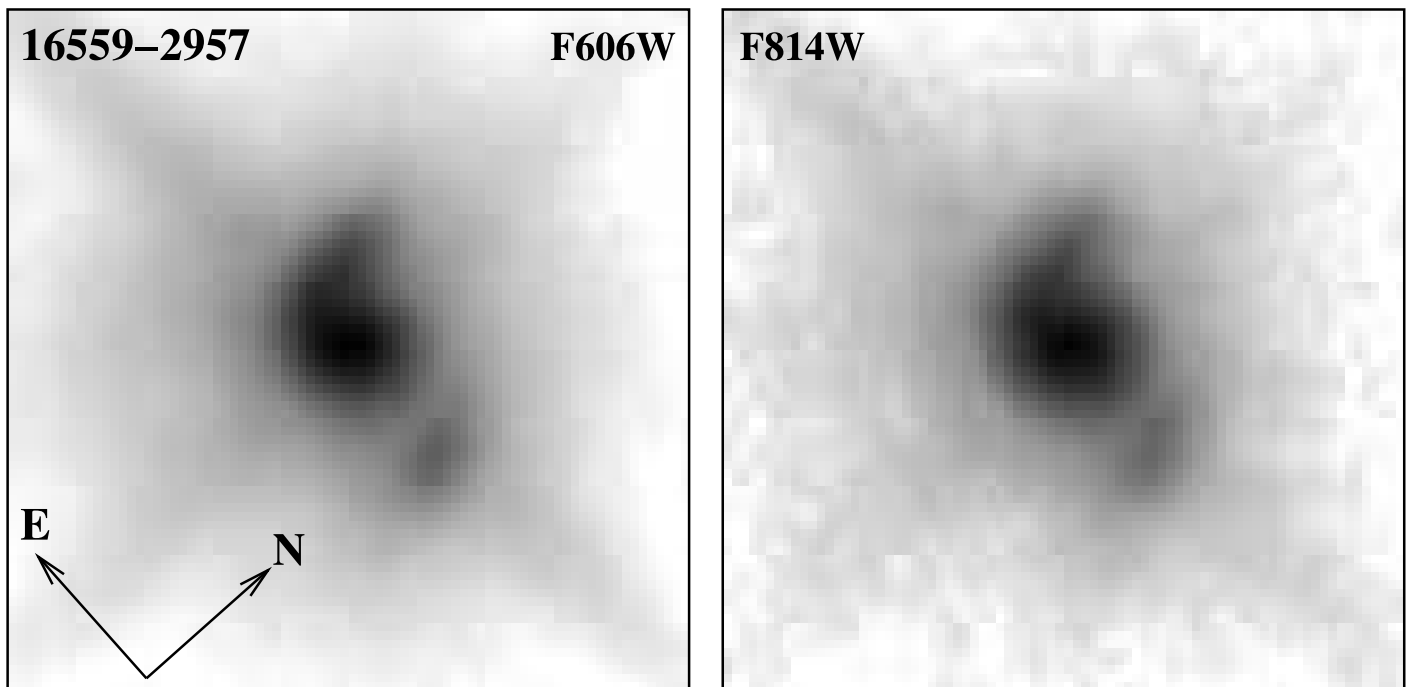


FIG. 8.— HST images (*log stretch*) of the young preplanetary nebula IRAS 16559-2957 ($1''.82 \times 1''.82$)

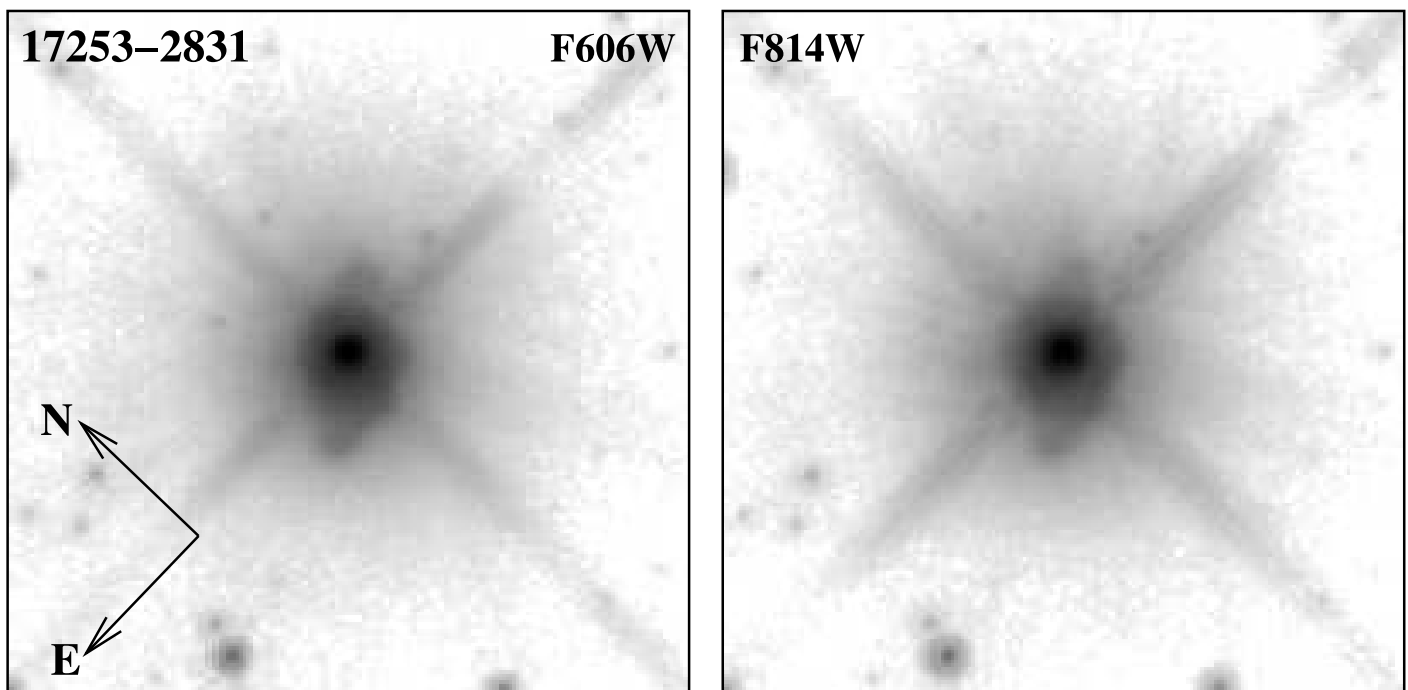


FIG. 9.— HST images (*log stretch*) of young preplanetary nebula IRAS 17253-2831 ($4''.57 \times 4''.57$)

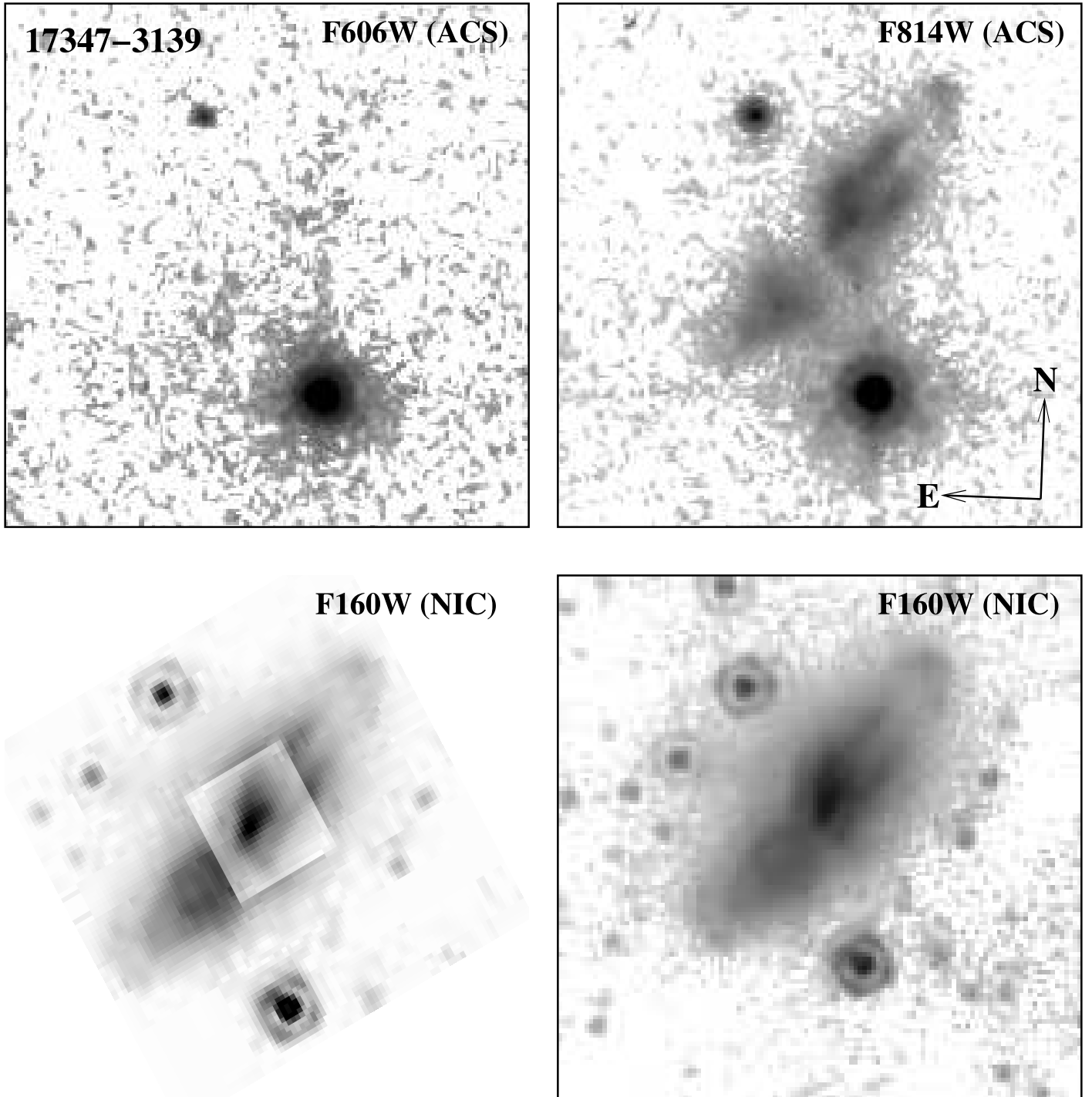


FIG. 10.— HST images of the young preplanetary nebula IRAS 17347-3139 ($5''.0 \times 5''.0$). The *top* panel shows ACS images using a *log stretch*. The *bottom* panel shows NICMOS (NIC1) images – on the *right* is the F160W image using a *log stretch*; on the *left* the same image is shown using a linear stretch, with the intensity reduced by a factor 5 in a central $0''.85 \times 0''.85$ patch, in order to better display the structure within the lobe. The faint patchy structure seen to the right of, and below the middle of, the nebula, in the F160W log-stretch image is an instrumental artifact.

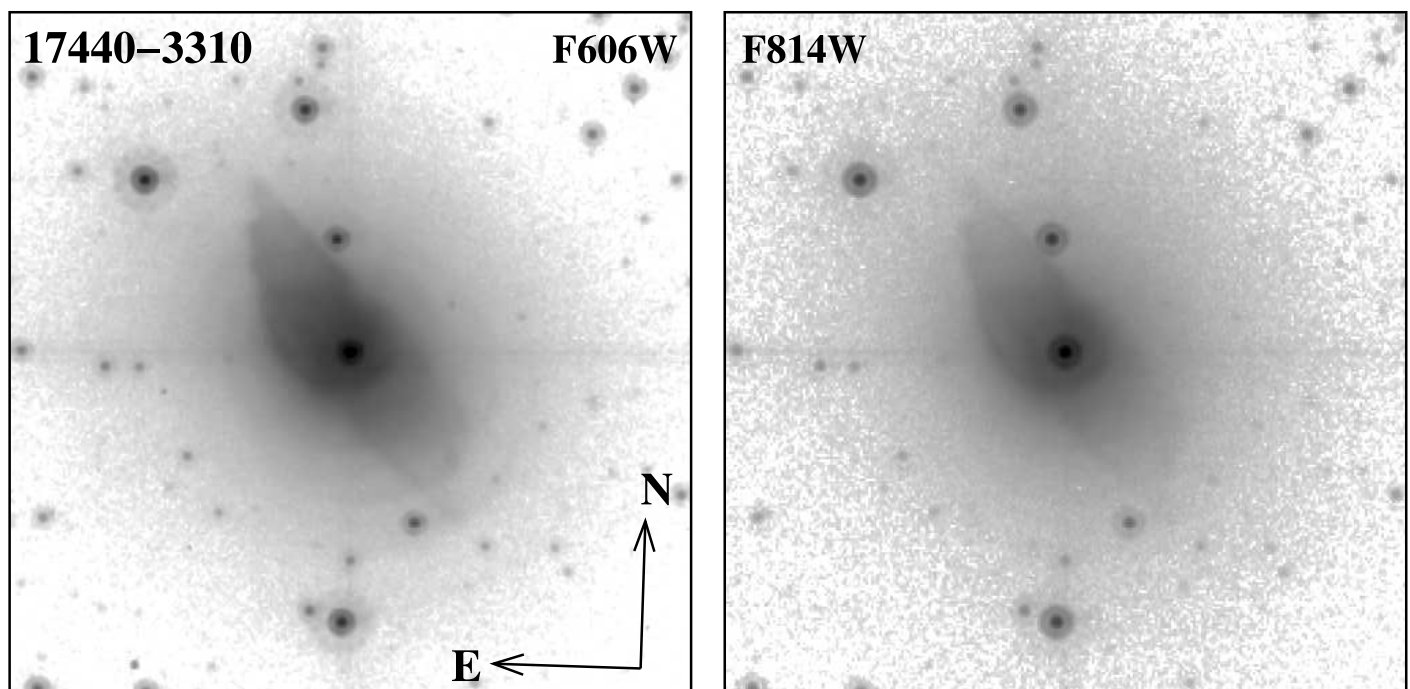


FIG. 11.— HST images (*log stretch*) of the young preplanetary nebulae IRAS 17440-3310 ($5''.0 \times 5''.0$).

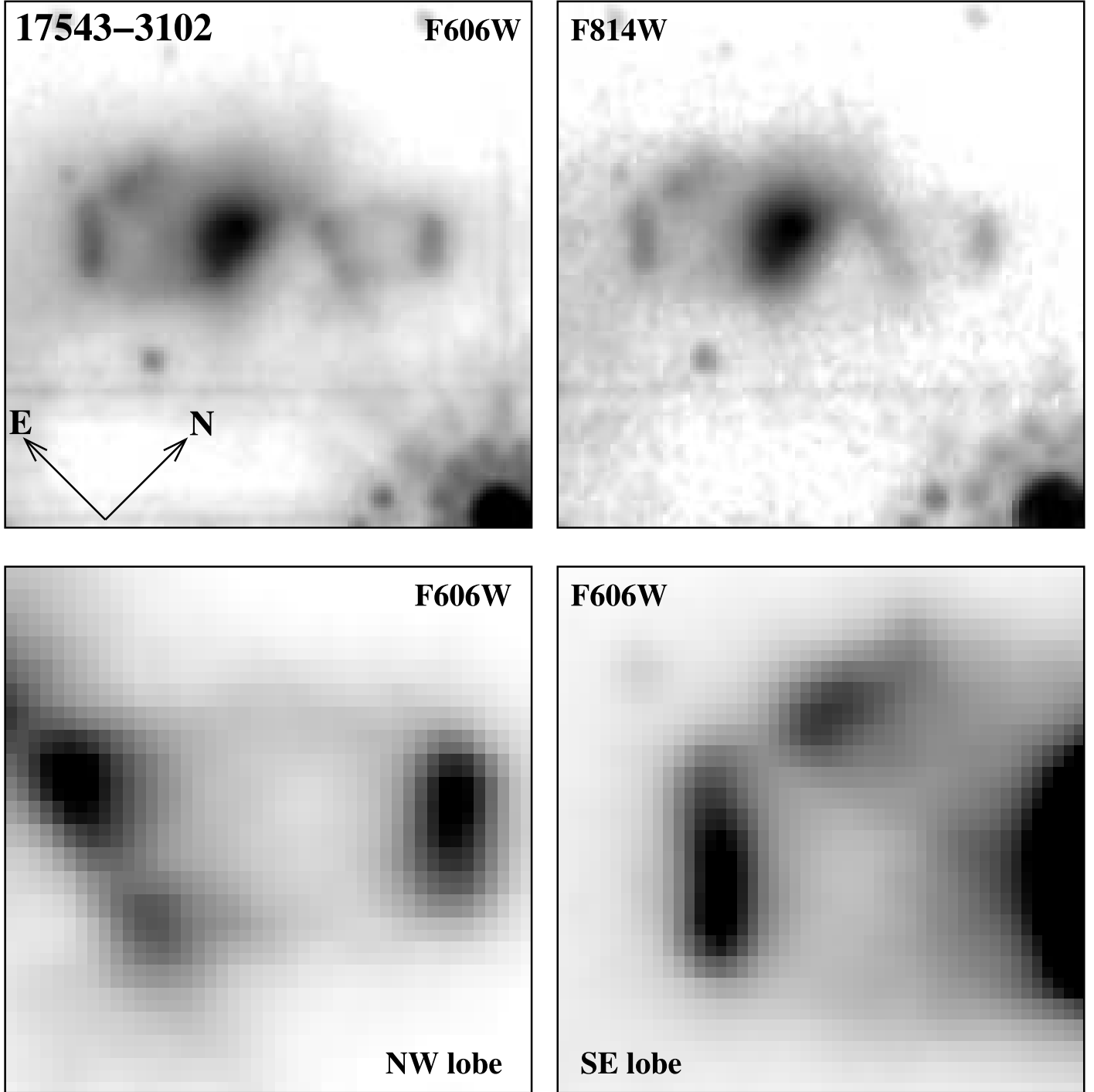


FIG. 12.— HST images of the young preplanetary nebulae IRAS 17543-3102 ($2''.0 \times 2''.0$). *Top* panel shows the F606W and F814 images on a *log stretch*, *bottom* panel shows magnified views ($0''.56 \times 0''.56$) of the SE and NW parts of the nebula in the F606W image on a linear stretch, with the central region saturated in order to bring out the shape and structure of the lobes

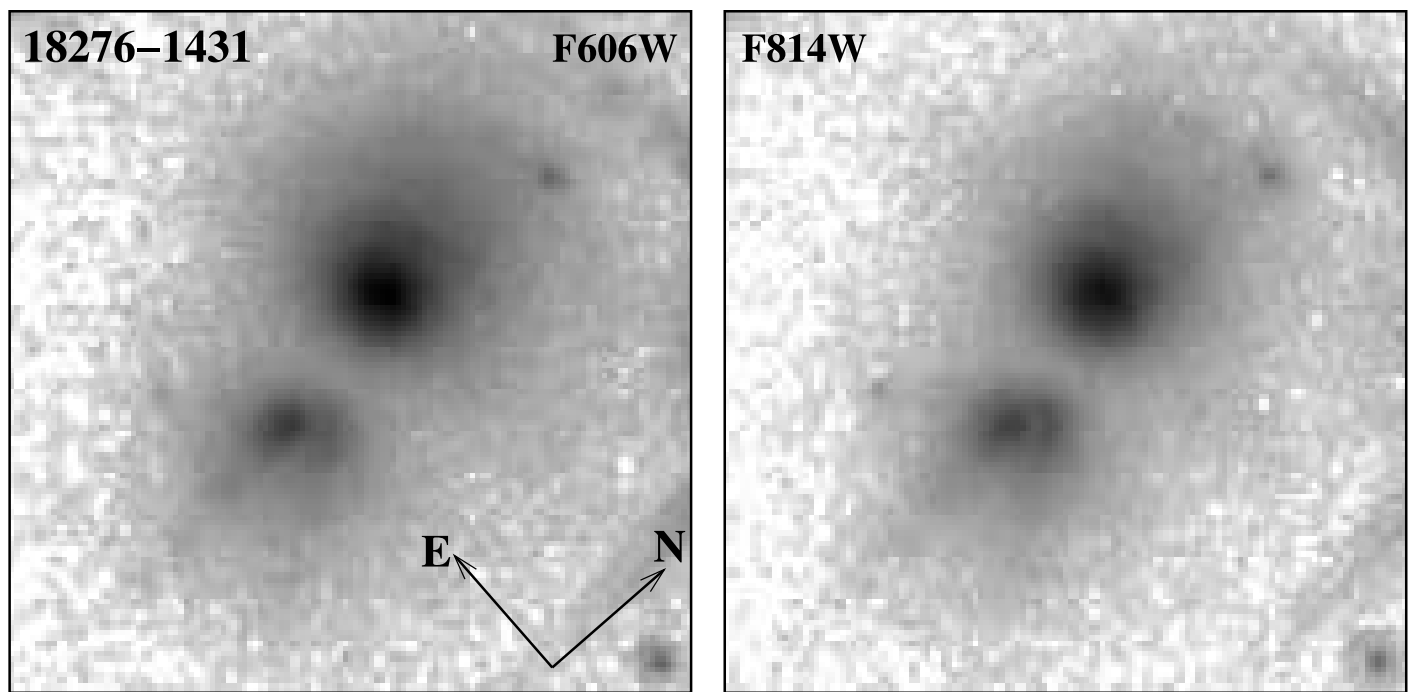


FIG. 13.— HST images (*log stretch*) of the young preplanetary nebula IRAS 18276-1431 ($2''.96 \times 2''.96$). The linear structures on the right edge of the image are diffraction spikes due to a bright field star.

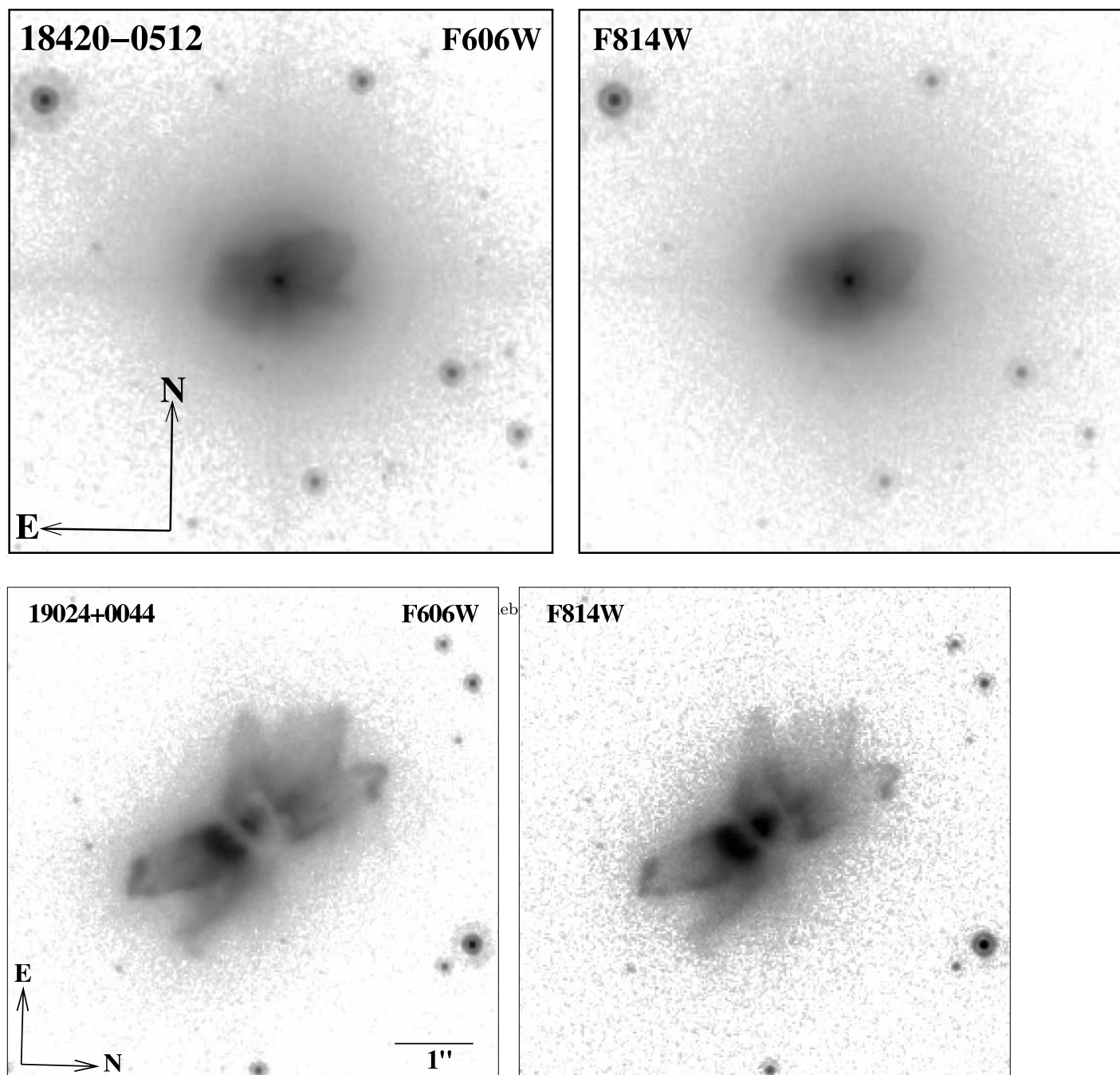


FIG. 15.— HST images (*log stretch*) of the young preplanetary nebula IRAS 19024+0044 ($6''.25 \times 6''.25$)

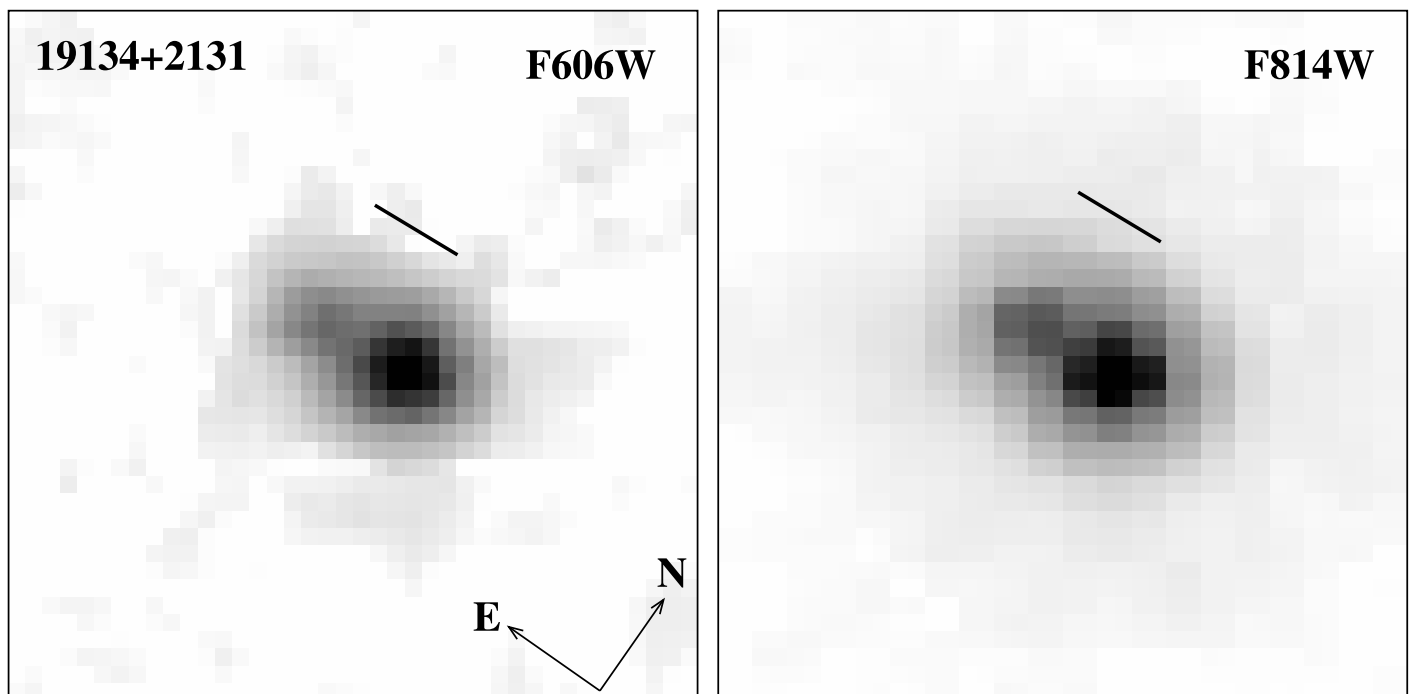


FIG. 16.— HST images (*square-root stretch*) of the young preplanetary nebula IRAS 19134+2131 ($1''.0 \times 1''.0$). The straight line segment shows the PA and separation of the blue- and red-shifted H_2O maser-jet spot clusters in this object observed by Imai et al. (2007).

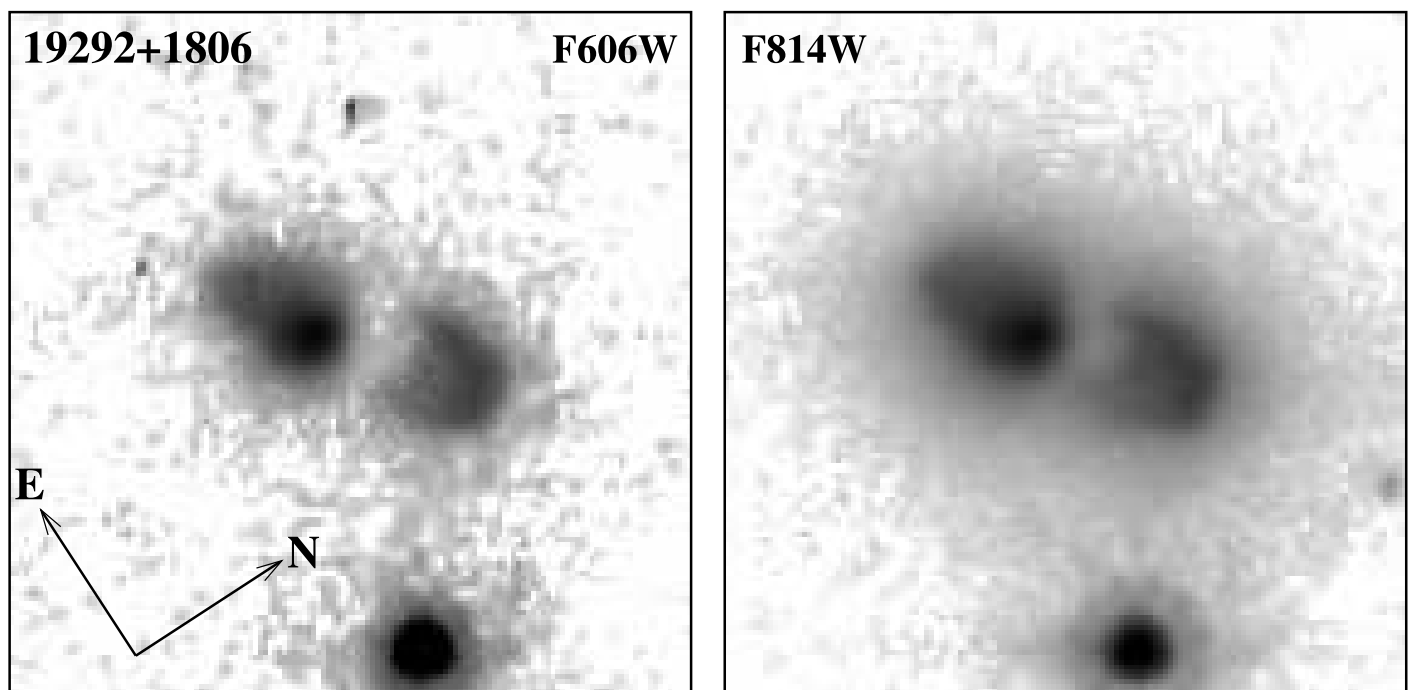


FIG. 17.— HST images (*log stretch*) of young preplanetary nebula IRAS 19292+1806 ($3''.5 \times 3''.5$).

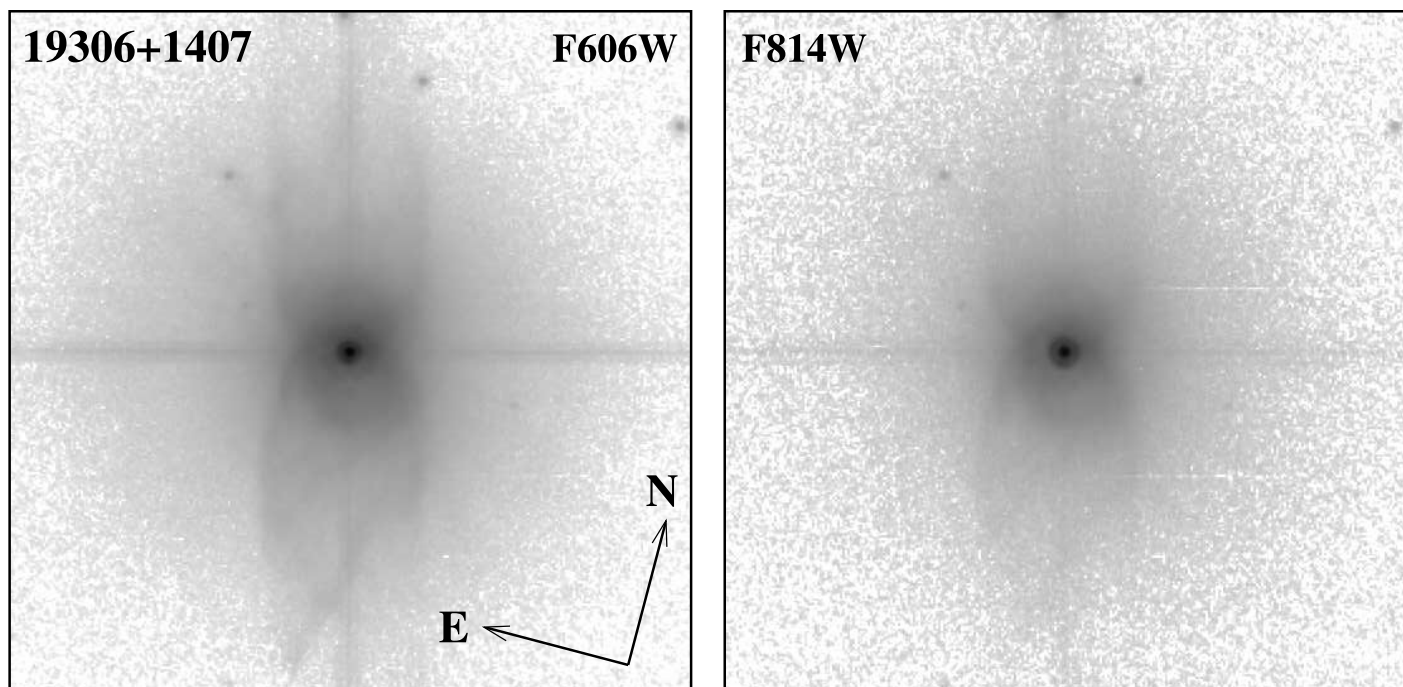


FIG. 18.— HST images (*log stretch*) of young preplanetary nebula IRAS 19306+1407 ($6''.75 \times 6''.75$).

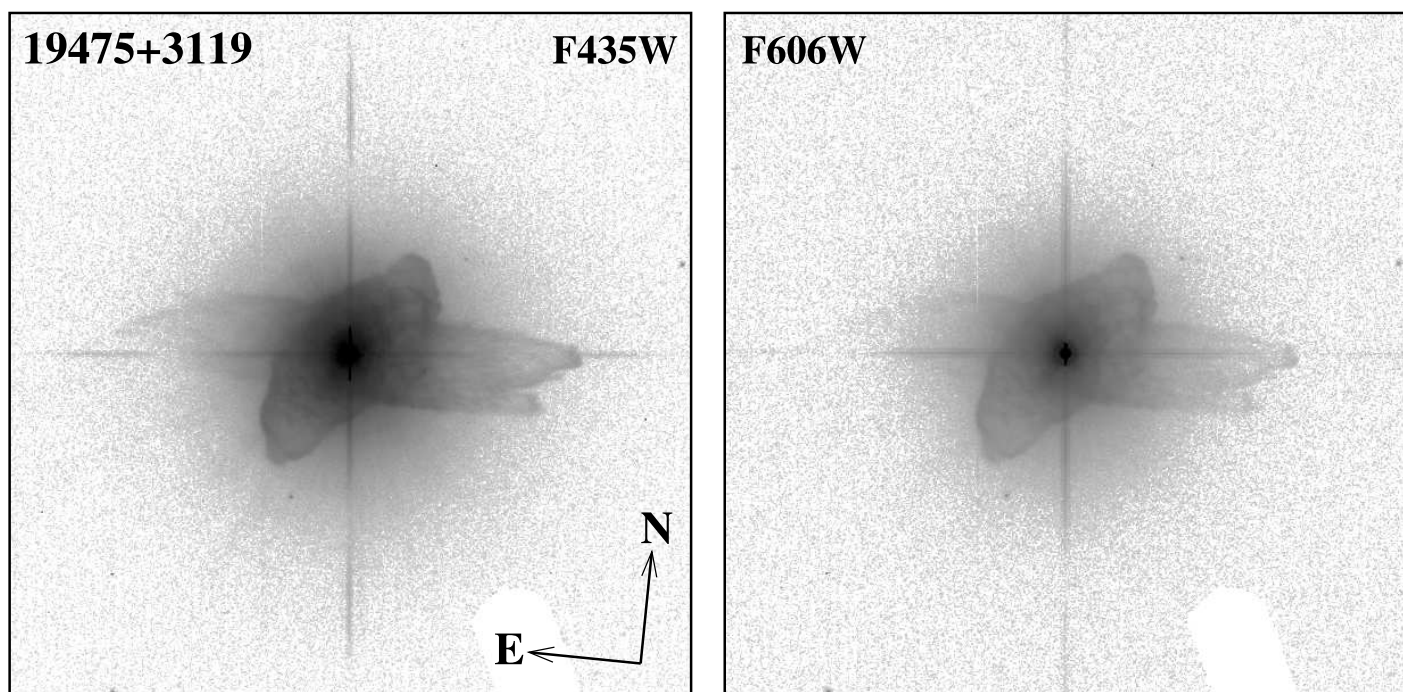


FIG. 19.— HST images (*log stretch*) of young preplanetary nebula IRAS 19475+3119 ($15''.0 \times 15''.0$)

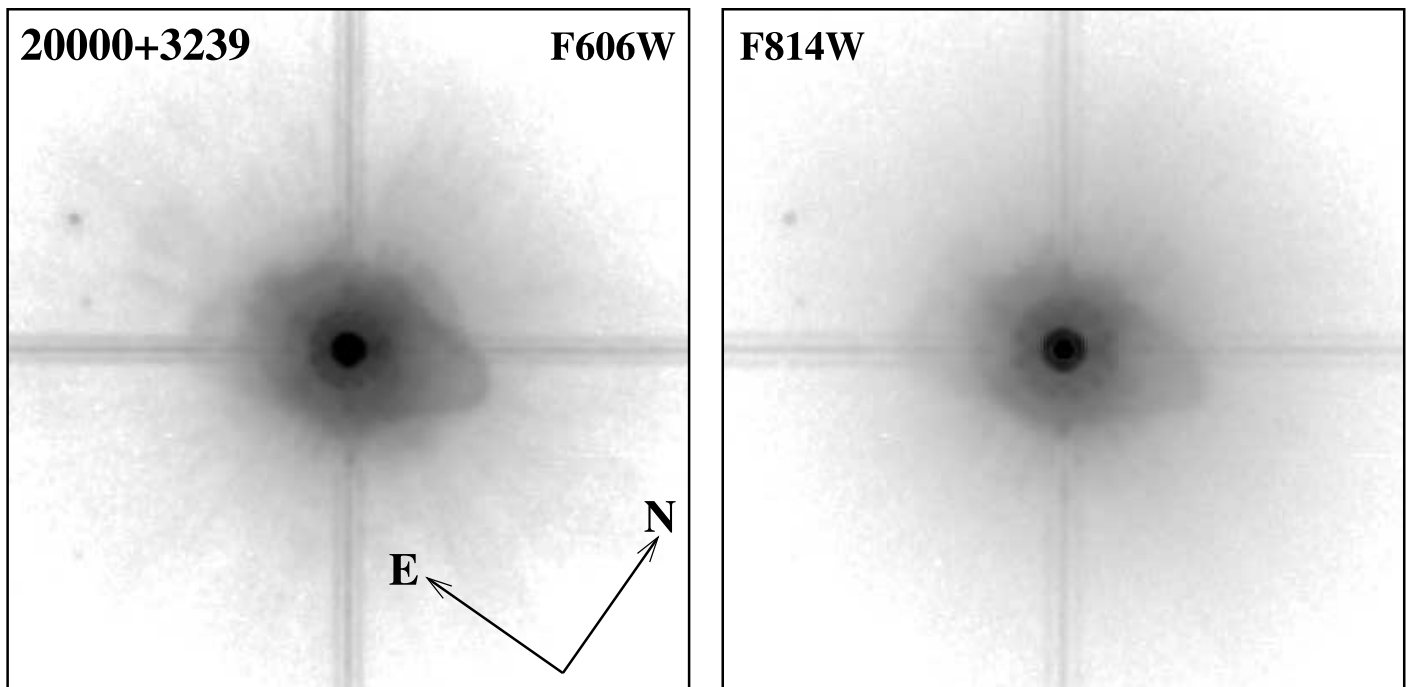


FIG. 20.— HST images (*log stretch*) of the young preplanetary nebula IRAS 20000+3239 ($5''.0 \times 5''.0$)

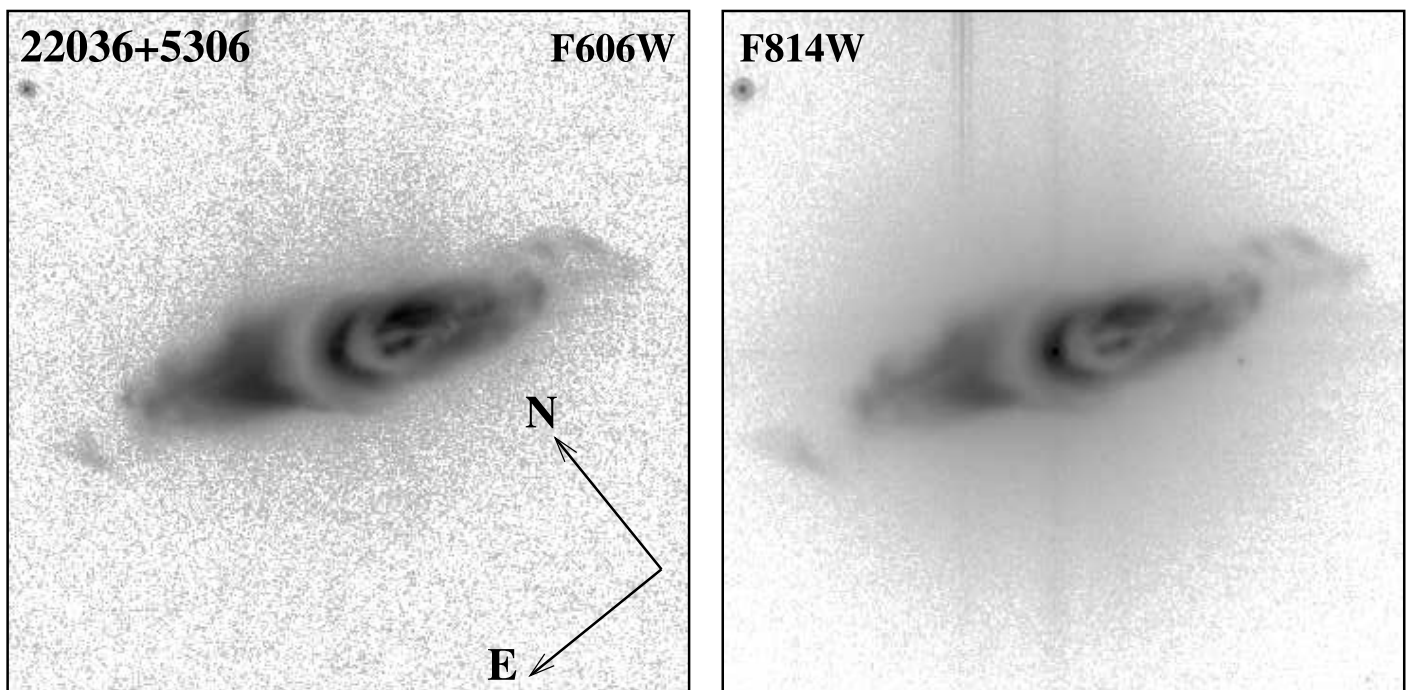


FIG. 21.— HST images (*log stretch*) of young preplanetary nebula IRAS 22036+5306 ($9''.0 \times 9''.0$). The vertical stripes are optical artifacts.

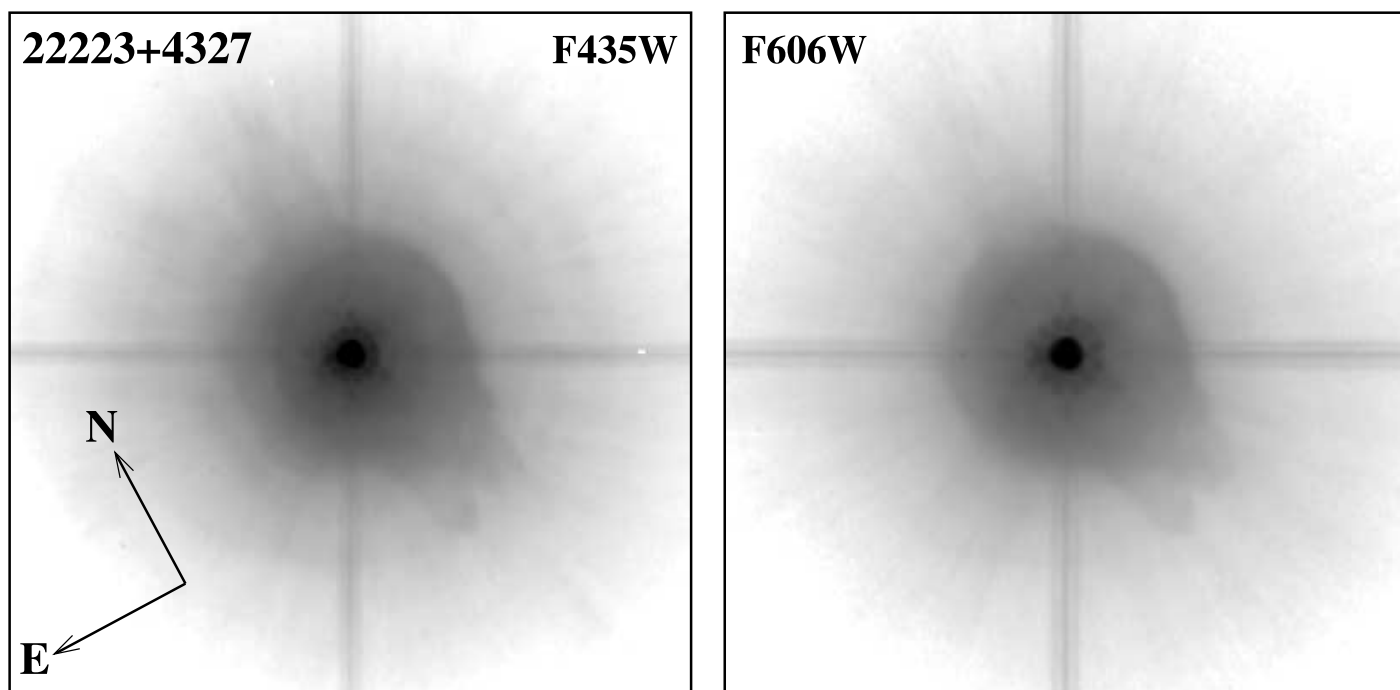


FIG. 22.— HST images (*log stretch*) of young preplanetary nebula IRAS 22223+4327 (5''0×5''0)

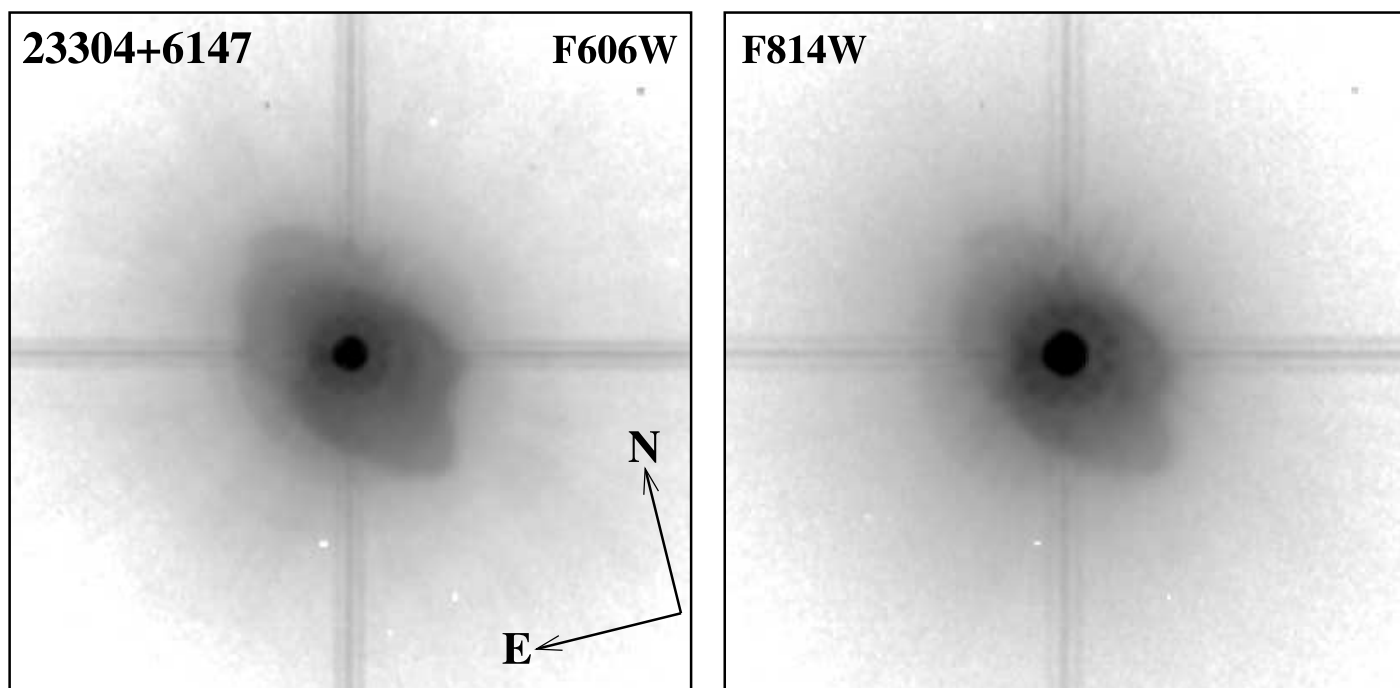


FIG. 23.— HST images (*log stretch*) of young preplanetary nebula IRAS 23304+6147 (5''0×5''0)

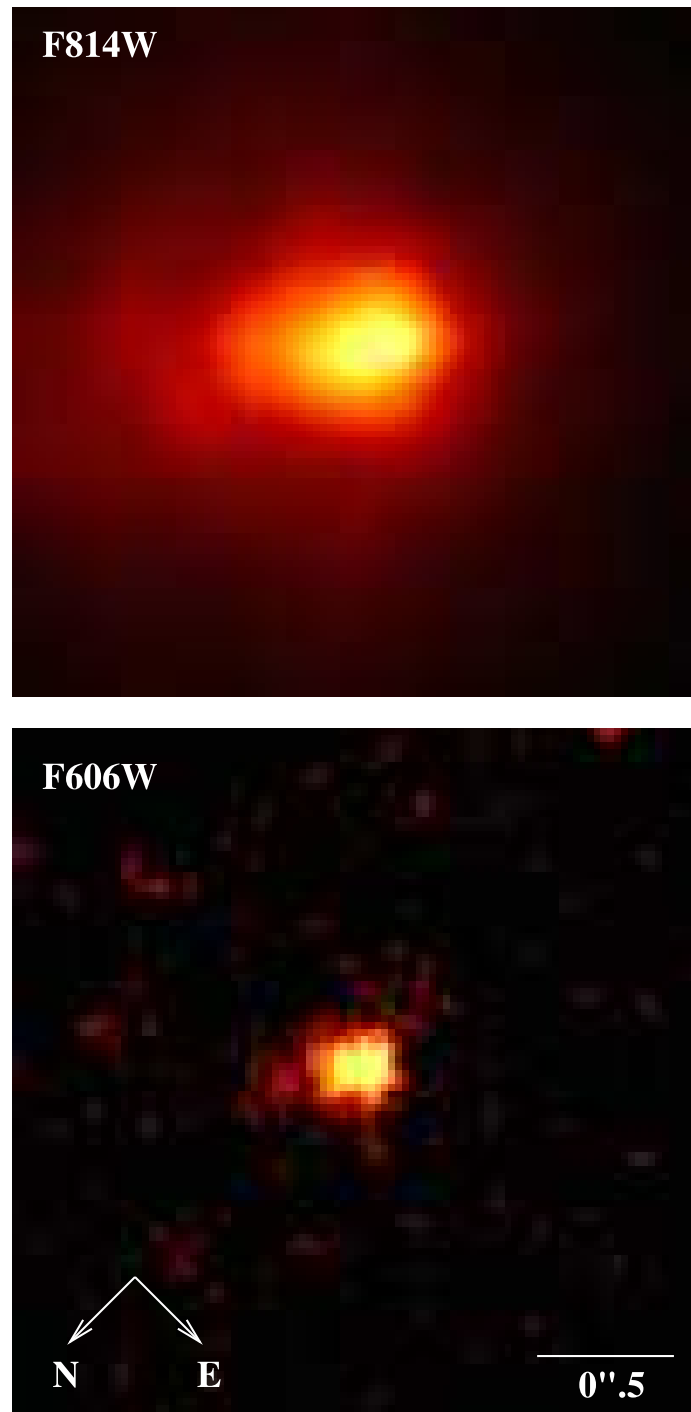


FIG. 24.— False-color HST images of the nascent preplanetary nebula IRAS 01037+1219 (*with sharp features enhanced*)

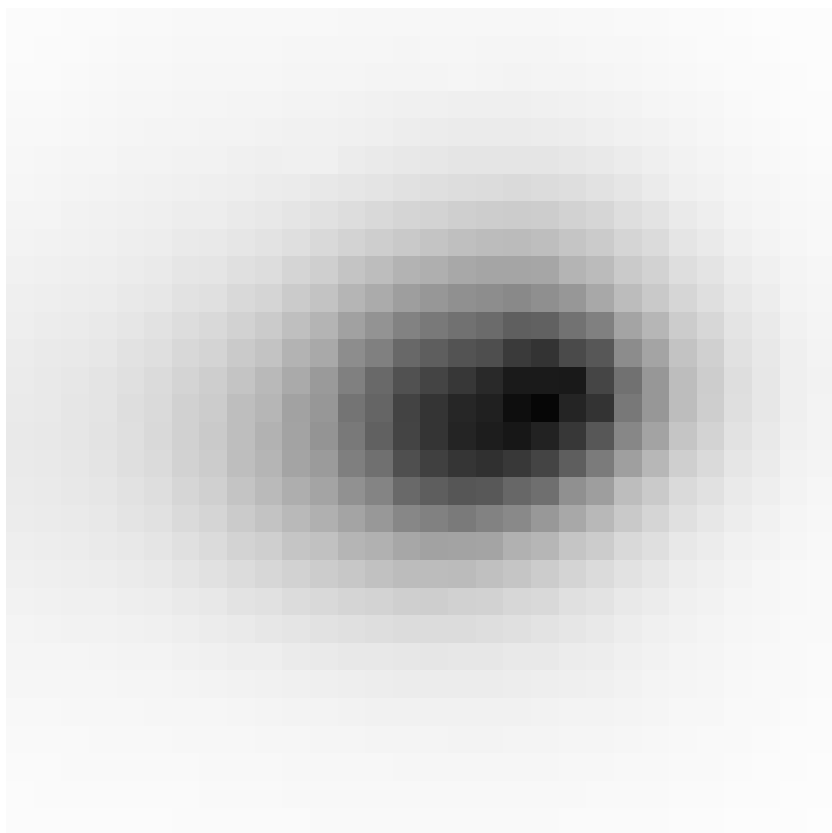


FIG. 25.— Expanded view of the central region ($0''.75 \times 0''.75$) of the nascent preplanetary nebula IRAS 01037+1219 (*linear stretch*)

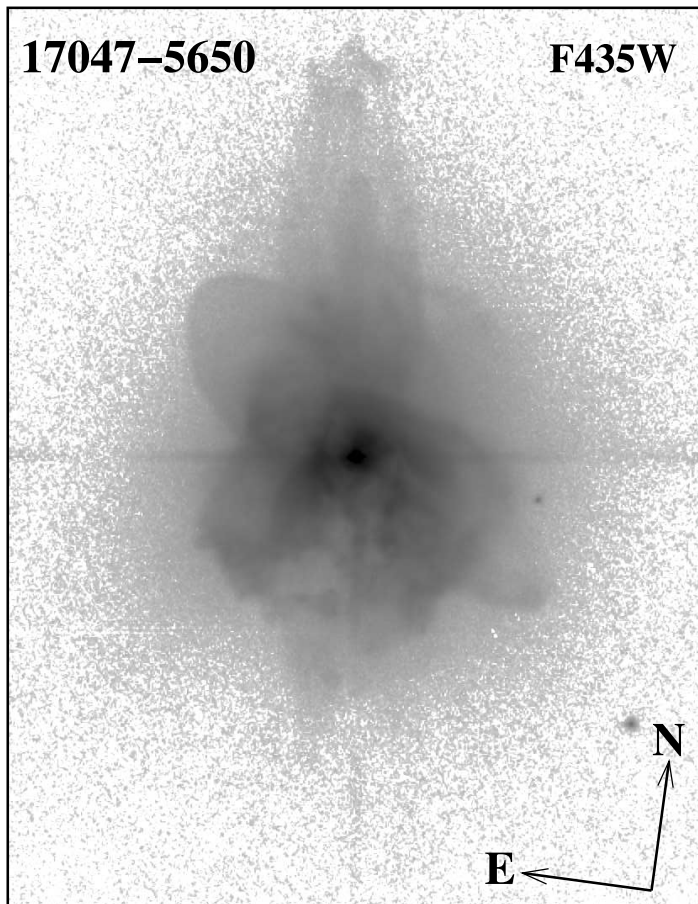


FIG. 26.— HST image (*log stretch*) of the young planetary nebula IRAS 17047-5650 ($10''.38 \times 13''.38$).

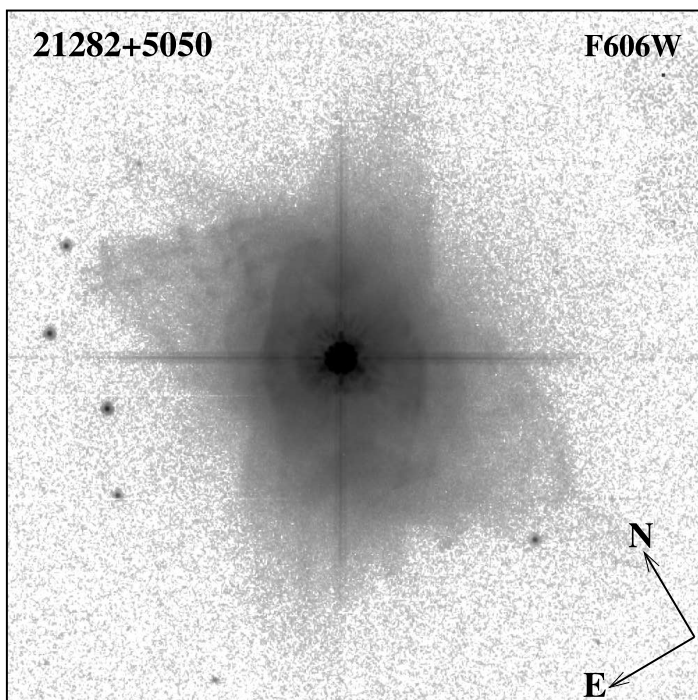


FIG. 27.— HST image (*log stretch*) of the young planetary nebula IRAS 21282+5050 ($12''.5 \times 12''.5$).

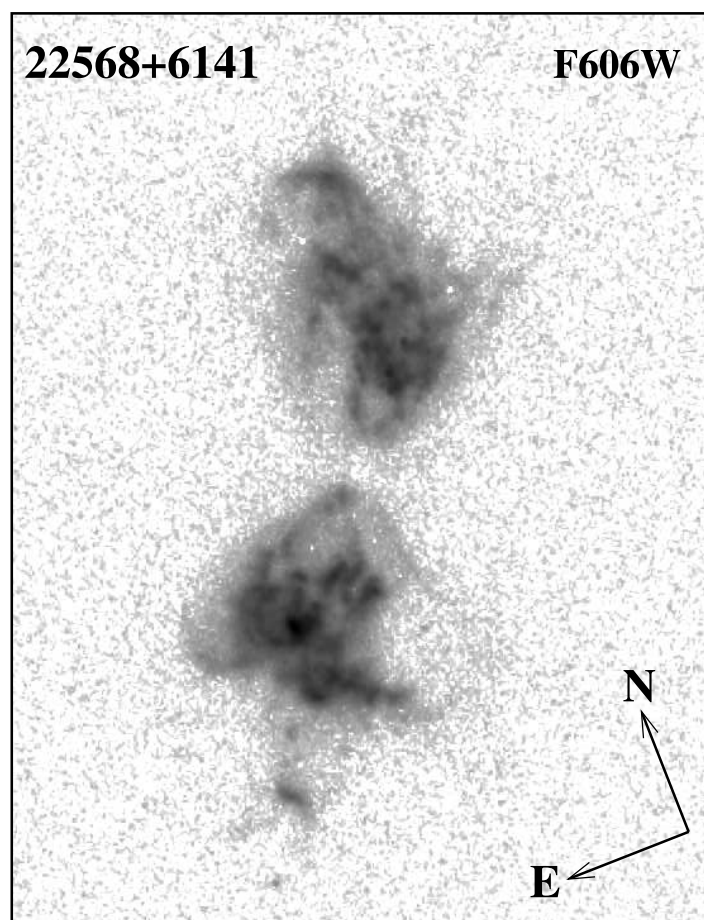


FIG. 28.— HST image (*log stretch*) of the young planetary nebula IRAS 22568+6141 ($6''.88 \times 9''.0$).

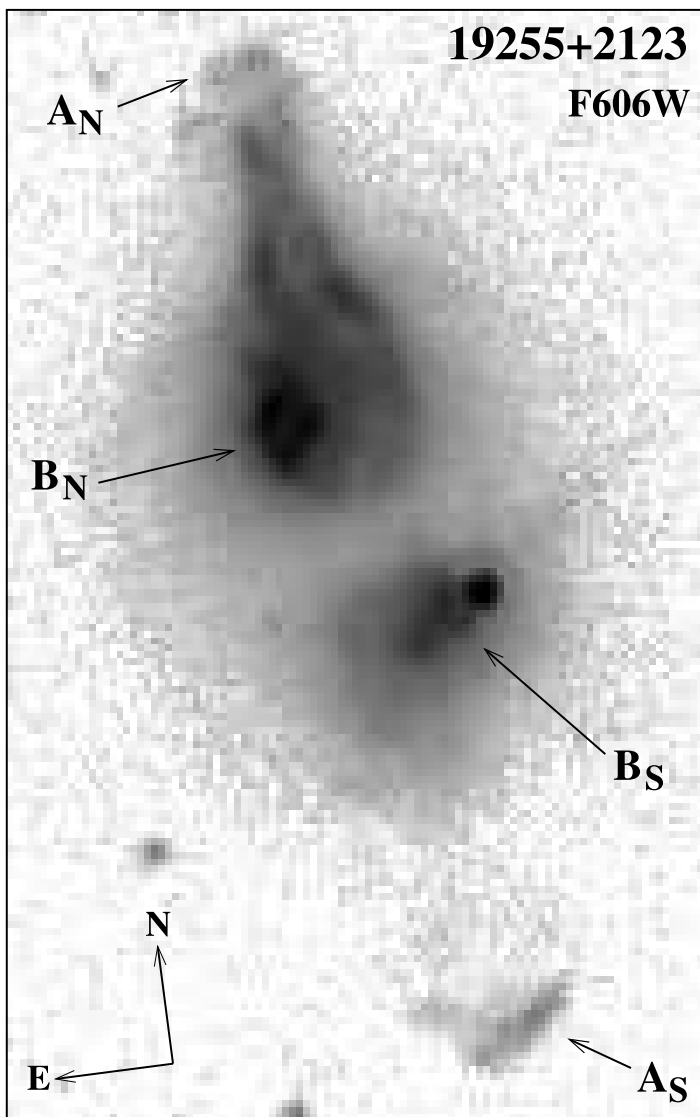


FIG. 29.— HST image (*log stretch*) of the young planetary nebula IRAS 19255+2123 ($4''.60 \times 7''.34$).

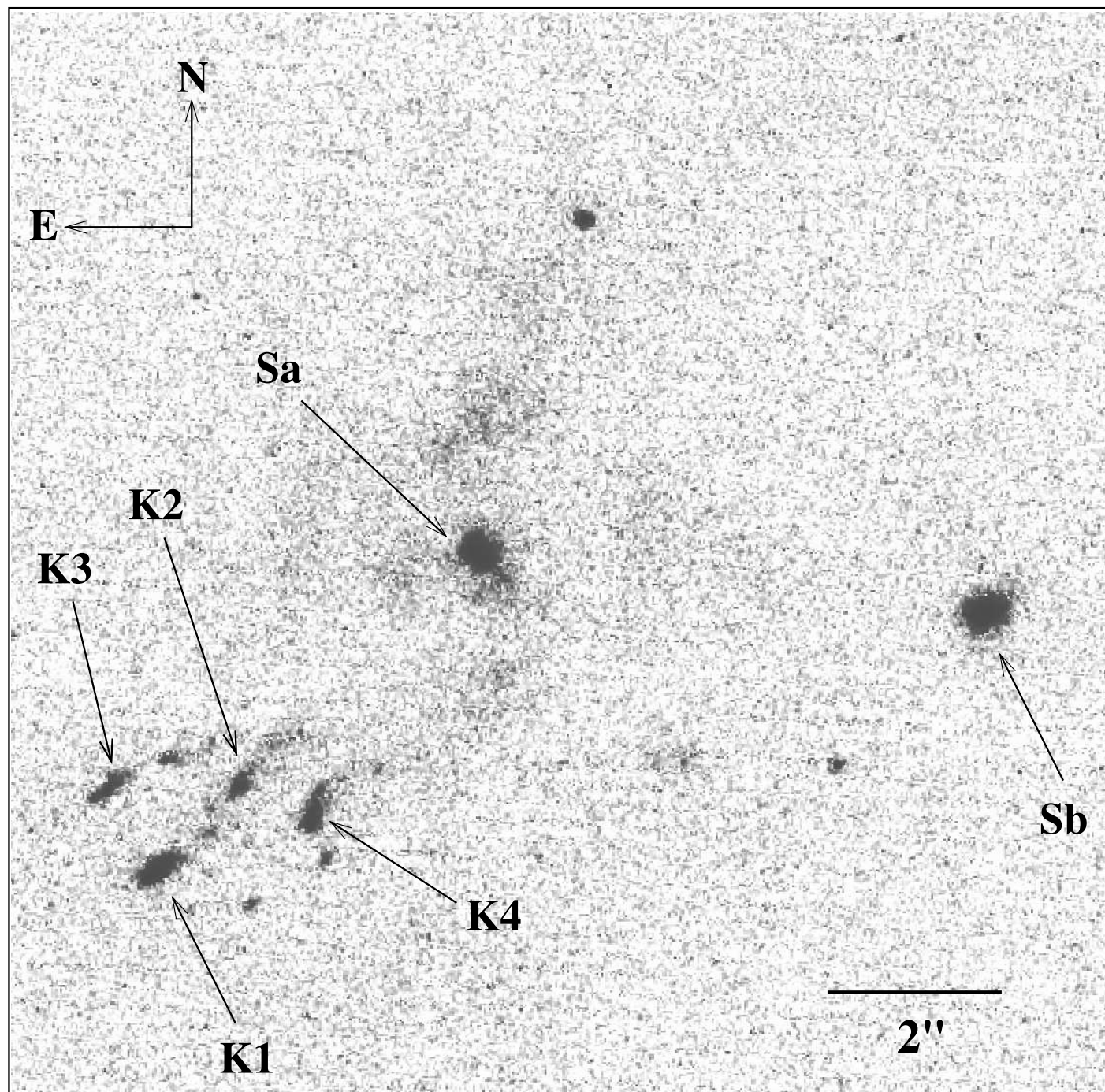


FIG. 30.— HST (F606W) image of IRAS 05506+2414.

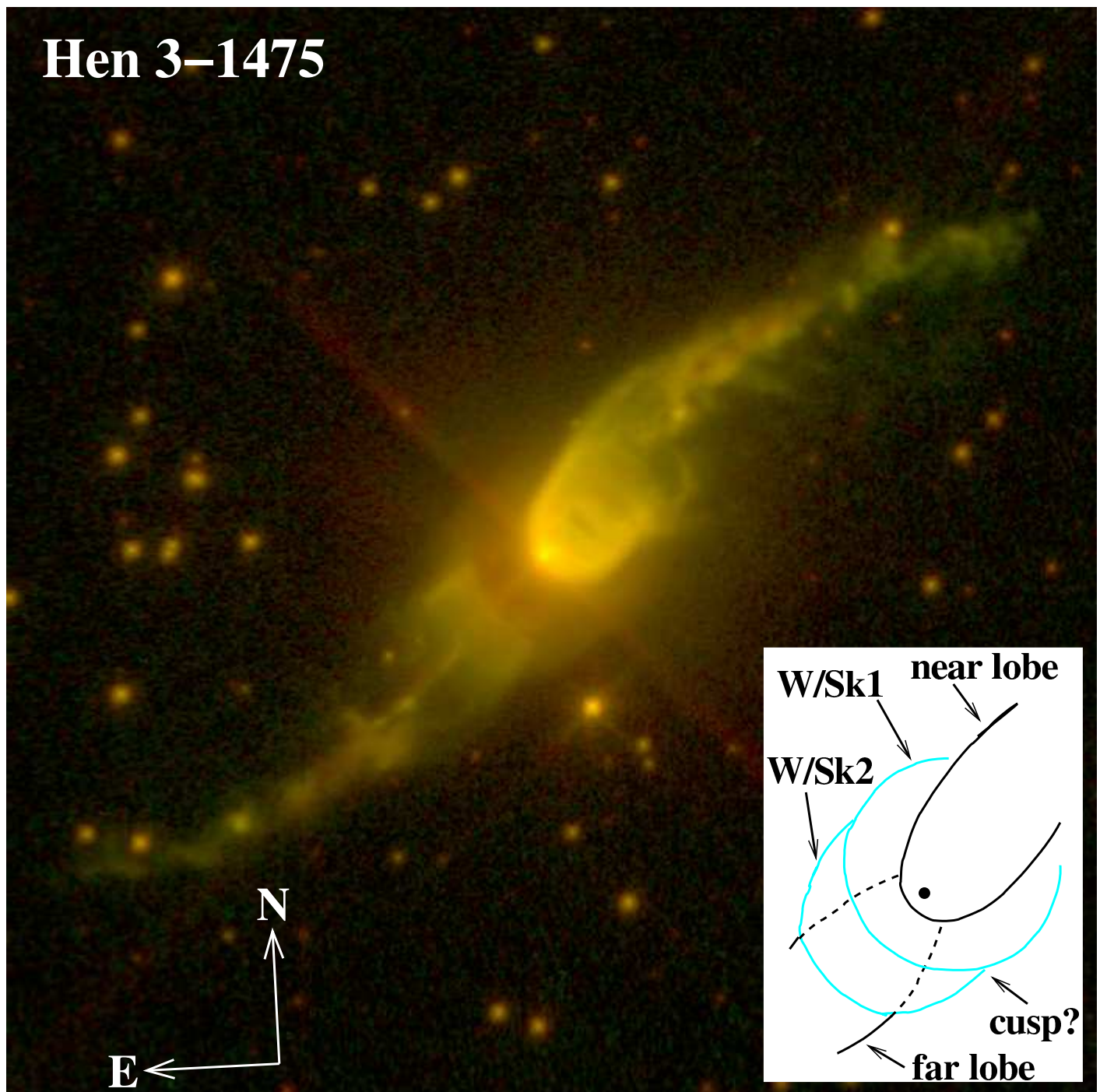


FIG. 31.— Color-composite (*green*: F555W, *red*: F814W) HST image of the pre-planetary nebula Hen 3-1475 ($18''.2 \times 18''.2$). Inset is a schematic of the central region, showing the outlines of the main structural features – background/shadowed features are shown as dashed curves. The cyan curves show the waist/skirt features whereas the black curves show the bipolar lobes.

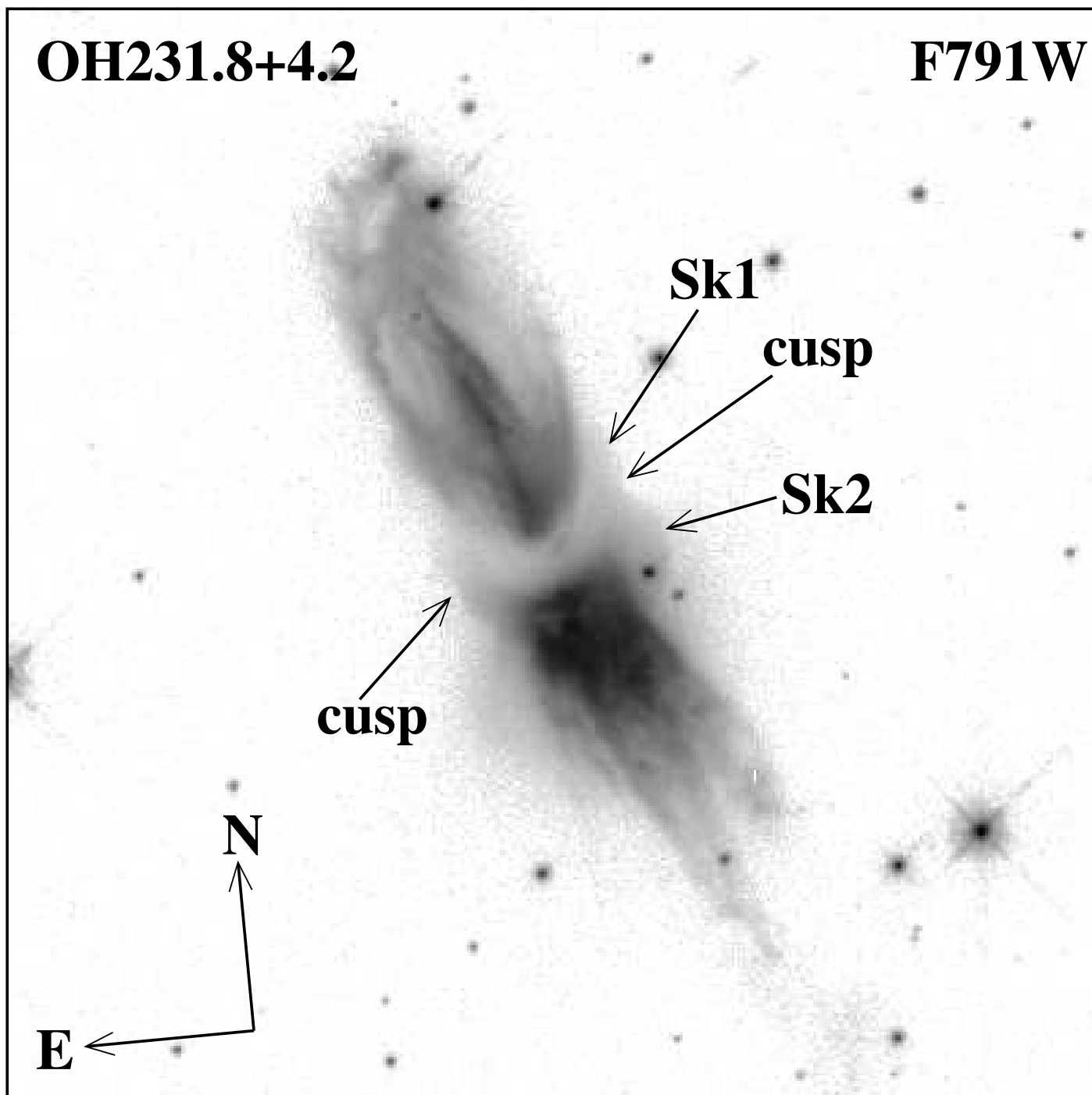


FIG. 32.— HST (F791W) image of the pre-planetary nebula OH231.8+4.2 ($39''.8 \times 39''.8$).

TABLE 1
SURVEY TARGETS

IRAS name	RA (2000) <i>hhmmss.ss</i>	DEC(2000) <i>ddmmss.s</i>	Chem.
Pre-Planetary Nebulae			
01037 + 1219 ^a	010625.98	+123553.0	O
11385 − 5517	114058.81	−553425.8	O
13428 − 6232	134620.54	−624759.6	−
13557 − 6442	135928.92	−645718.3	O
15405 − 4945	154411.06	−495522.1	O
15452 − 5459	154911.38	−550851.6	O
15553 − 5230	155911.18	−523841.6	−
16559 − 2957	165908.22	−300140.3	O
17253 − 2831	172832.96	−283325.8	O
17347 − 3139	173800.61	−314055.2	O
17440 − 3310	174722.72	−331109.3	O
17543 − 3102	175733.61	−310303.5	O
18276 − 1431	183030.70	−142857.0	O
18420 − 0512	184441.65	−050917.0	O
19024 + 0044	190502.06	+004850.9	O
19134 + 2131	191535.21	+213634.0	O
19292 + 1806	193125.37	+181310.3	O
19306 + 1407	193255.08	+141336.9	C+O
19475 + 3119	194929.56	+312716.3	O
20000 + 3239	200159.52	+324732.9	C
22036 + 5306	220530.29	+532132.8	O
22223 + 4327	222431.43	+434310.9	C
23304 + 6147	233244.79	+620349.1	C
Other Objects			
05506 + 2414 ^b	055343.56	+241444.7	
17047 − 5650 ^c	170900.93	−565448.0	
19255 + 2123 ^c	192744.02	+213003.4	
21282 + 5050 ^c	212958.47	+510400.3	
22568 + 6141 ^c	225854.89	+615758.0	

^anascent pre-planetary nebula

^bmost likely a young stellar object

^cplanetary nebula

TABLE 2
MORPHOLOGICAL CLASSIFICATION CODES

PRIMARY CLASSIFICATION – <i>Nebular Shape</i>	
B	Bipolar
M	Multipolar
E	Elongated
I	Irregular
SECONDARY CLASSIFICATIONS	
<i>lobe shape:</i>	
o	lobes open at ends
c	lobes closed at ends
<i>obscuring waist:</i>	
w	central obscuring waist
w(b)	obscuring waist has sharp radial boundary
<i>central star:</i>	
★	central star evident in optical images
<i>other nebular characteristics:</i>	
an	ansae present
ml	minor lobes are present
sk	a skirt-like structure present around the primary lobes
<i>point symmetry:</i>	
ps(m)	two or more pairs of diametrically-opposed lobes
ps(an)	diametrically-opposed ansae present
ps(s)	overall geometric shape of lobes is point-symmetric
<i>halo:</i>	
h	halo emission is present (relatively low-surface brightness diffuse region around primary nebular structure)
h(e)	halo has elongated shape
h(i)	halo has indeterminate shape
h(a)	halo has centro-symmetric arc-like features
h(sb)	searchlight-beams are present

TABLE 3
PROPERTIES OF SURVEY PRE-PLANETARY NEBULAE

IRAS name	f25/f12	Morphology	r_{PAGB} (")	t_{PAGB} (yr)	r_{AGB} (")	V_{exp} km s ⁻¹	t_{AGB} (yr)	T_d (K)	M_d 10 ⁻³ M_\odot	Dist. (kpc)
01037 + 1219 ^a	0.83	E	35	20	5500	...	1.3	0.65
11385 - 5517	1.5	I	4.6	180	(4.6)	(15)	1800	74	1.3	1.2
13428 - 6232	15.4	Bow	24.7	1470	(24.7)	(15)	14700	88	2.9	1.9
13557 - 6442	1.9	Bow,h	0.8	85	3.0	(15)	3500	103	0.53	3.3
15405 - 4945	>11	Bcw,ps(s),h(e)	1.0	155	3.0	13.5	5200	72	7.0	4.9
15452 - 5459	2.9	Bow	11.7	625	(11.7)	9.5	9850	87	1.8	1.7
15553 - 5230	4.9	Bow	1.1	145	(1.1)	(15)	1430	104	1.1	4.3
16559 - 2957	3.5	Bw,ps(s),h	0.35	60	3.5	14.8	5850	118	0.38	5.2
17253 - 2831	15.1	Ec*,ps(s),h	0.66	160	2.7	9.1	10800	98	1.5	7.7
17347 - 3139	5.3	Bcw,h(e)	1.9	185	2.0	(15)	1950	81	3.2	3.1
17440 - 3310	>5.1	Bc*,ps(s),h(a)	1.4	335	4	14.6	9850	79	5.5	7.6
17543 - 3102	7.9	Bc,an,h(i)	1.35	310	2	(15)	4600	83	3.6	7.3
18276 - 1431 ^b	5.8	Bcw,h(e,a,sb)	0.5	45	2.8	17.0	2300	50-105	4.75	3
18420 - 0512	25.9	Ec*,h(a)	0.8	170	3	12.4	7600	88	2.6	6.6
19024 + 0044	17.1	Mcw(b),an,ps(m,an),h	1.8	440	2	13.4	3700	109	1.2	5.1
19134 + 2131	3.1	Bcw	0.12	30	(0.12)	(15)	300	69	2.7	8.4
19292 + 1806	>9.6	Bcw(b),h(e)	0.9	150	2.5	14.6	4250	103	1.1	5.2
19306 + 1407	16.4	Bo*,h	3.2	500	4	14	6650	99	1.3	4.9
19475 + 3119 ^c	70.4	Mc*,ps(m,s),h	5.2	1660	6	15	8000	46-94	4.3	4.2
20000 + 3239	4.7	Ec*,h	1.0	110	5	12.3	6850	103	0.88	3.5
22036 + 5306	5.5	Bcw(b),an,ps(s,an),h	4.0	255	6.5	7	8850	35-50	23.5	2
22223 + 4327	17.5	Ec*,h(a)	1.5	204	7.5	14	11000	99	0.79	4.3
23304 + 6147	5.2	Mc*,ps(m),h(a)	1.1	145	5.5	15.5	7000	99	0.82	4.2

^avalues of r_{AGB} , t_{AGB} , M_d , Dist from Vinkovic et al. 2004

^bvalues of parameters from Sánchez-Contreras et al. (2007), scaled appropriately for $L=6000L_\odot$ as necessary

^cvalues of parameters from Sahai et al. (2007) and Sánchez Contreras et al. 2006, scaled appropriately for $L=6000L_\odot$ as necessary

Note. — Numbers in parenthesis imply *assumed* values

TABLE 4
PROPERTIES OF PREVIOUSLY OBSERVED, WELL-RESOLVED PRE-PLANETARY NEBULAE

IRAS name	f25/f12	Imaging Refs.	Chem. ^a	Morphology
<i>Well-Studied PPNs</i>				
AFGL 618 ^b	2.3	1	C	Mcw,ml,h(e,a)
Red Rectangle	1.1	2	C+O	Bow
OH 231.8 + 4.2	11.9	3	O	Bcw,sk
07131 – 0147	1.6	4	O	Bow*
Frosty Leo Neb.	>17	5	O	Bcw(b)*,an,ml,ps(m,an,s)
Roberts 22	5.5	6	C+O	Bcw,ml,ps(s),h(e)
Hen 3-401	9.3	7	C	Bow*,sk
Boomerang Neb.	1.3	8	...	Bow*
16342 – 3814	12.3	9	O	Bcw,ps(s)
Hen 3-1475	4.0	10	O	Bow(b)*,an,sk,ps(an,s),h
M 1-92	3.4	11	O	Bcw(b)*,an
AFGL 2688	...	12	C	Bcw(b),ml,h(e,a,sb)
<i>Less Well-Studied PPNs</i>				
02229 + 6208	3.1	10	C	E
04296 + 3429	3.6	13	C	Bcw(b),h
05341 + 0852	2.2	10	C	Ec*,ps(s),h
06530 – 0213	4.5	10	C	Bc*,ml,ps(s),h(e)
07134 + 1005	4.8	10	C	Ec*,h(e)
07430 + 1115	3.9	10	C	E*,h
08005 – 2356	2.9	10	O	Bc*
16594 – 4656	6.6	14	C	Mcw*,an,ps(m,an),h(a)
17106 – 3046	15.5	15	O	Bw(b)
17150 – 3224	5.6	16	O	Bcw,h(a,sb)
17245 – 3951	13.3	14	O	Bcw,h(sb)
17436 + 5003	30.1	10	O	Ec*
17441 – 2411	4.5	17	C	Bcw,h(e,a)
18095 + 2704	2.8	10	O	Bc,h
19374 + 2359	4.2	10	O	B,h(e)
19477 + 2401	4.9	14	C	E,h(e)
20028 + 3910	5.0	18	C	Bcw(b),h(e,a,sb)
22272 + 5435	4.1	10	C	Ec*,h(a)
22574 + 6609	3.3	14	C	Bwh(i)
23321 + 6545	6.3	10	C	Ec

^aInformation about the nebular chemistry has been taken either directly (in most cases) from the imaging reference paper, or from papers cited in the latter

^bThe “a” descriptor is based on an unpublished HST/ACS F606W image provided by Dr. Bruce Balick (Huehnerhoff, Baerny, & Balick, in preparation) using data from GO 9430/PI S. Trammell

References. — *References for HST Images* 1: Lee & Sahai 2003; 2: Cohen et al. 2004, 3: Bujarrabal et al. 2002, 4: Scarrott et al. 1990 (*ground-based image only*), 5: Sahai et al. 2000a, 6: Sahai et al. 1999d, 7: Sahai et al. 1999a, 8: Sahai et al. 2000b, 9: Sahai et al. 1999b, 10: Ueta et al. 2000, 11: Bujarrabal et al. 1998, 12: Sahai et al. 1998a, 13: Sahai 1999, 14: Su et al. 2001, 15: Kwok et al. 2000, 16: Kwok, Su & Hrivnak 1998, 17: Su et al. 1998, 18: Hrivnak, Kwok, & Su 2001, 19: Su, Hrivnak, & Kwok 2001